# Inter–annual global carbon cycle variations linked to atmospheric circulation variability

Na Li[1], Sebastian Sippel[2], Alexander J. Winkler[1], Miguel D. Mahecha[3], Markus Reichstein[1], and Ana Bastos[1]

[1]Max Planck Institute for Biogeochemistry, Germany
[2]Institute for Atmospheric and Climate Science, and Seminar for Statistics, ETH Zurich, Switzerland
[3]Remote Sensing Center for Earth System Research, Leipzig University, Germany

**Correspondence:** Na Li (nali@bgc-jena.mpg.de)

**Abstract.**

One of the least understood temporal–scales of global carbon cycle (C–cycle) dynamics is its inter–annual variability (IAV). This variability is mainly driven by variations in the local climatic drivers of terrestrial ecosystem activity, which in turn are controlled by large–scale modes of atmospheric variability. Here, we quantify the fraction of C–cycle IAV that is explained

5 by large–scale atmospheric circulation variability, which is quantified by spatio–temporal sea level pressure (SLP) fields. $CO_2$ variability is diagnosed from the detrended atmospheric $CO_2$ growth rate and the land $CO_2$ sink from different datasets in the global carbon budget. We use a regularized linear regression model, a statistical learning technique, apt to deal with the large number of atmospheric circulation predictors ($p \geq 800$, each representing one pixel–based time–series of SLP anomalies) in a relatively short observed record ($n < 60$ years). We show that boreal winter and spring SLP anomalies allow predicting IAV

10 in atmospheric $CO_2$ growth rate and of the global land sink, with Pearson correlations between reference and predicted values as high as 0.70–0.84 with boreal winter SLP anomalies. This is comparable or higher than that of a similar model using 15 traditional teleconnection indices as predictors. The coefficient patterns of the model based on SLP fields show a predominant role of the tropical Pacific and over Southeast Asia extending to Australia, corresponding to the regions associated with the El Niño/Southern Oscillation variability. We also identify one region in the western Pacific, roughly corresponding to the West

15 Pacific pattern.

We further evaluate the influence of the time–series length on the predictability of IAV and find that reliable estimates of C–cycle IAV can be obtained from records of ∼30–60 years. For shorter time–series ($n < 30$ years), however, conclusions about $CO_2$ IAV patterns and drivers need to be evaluated with caution. Overall, our study illustrates a new data–driven and flexible approach to model the relationship between large–scale atmospheric circulation variations and C–cycle variability at

20 global and regional scales, complementing the traditional use of teleconnection indices.

## 1 Introduction

All processes in the global carbon cycle (C–cycle) vary at multiple time scales ranging from minutes to millennium (IPCC, 2013). Quantifying and understanding the patterns of variability in the C–cycle and their drivers is crucial to better understand

the drivers of C–cycle dynamics and better constrain future climate projections (Cox et al., 2013; Friedlingstein et al., 2014).
25    Primarily driven by the land sink dynamics (Piao et al., 2020), inter–annual variability (IAV) is one of the most uncertain and poorly understood terms of the global C–cycle in the observational period (Friedlingstein et al., 2019).

A fundamental challenge is that variability in land–atmosphere carbon exchange is affected in complex ways by atmosphere–ocean climate variability but also land use changes, forced climate changes, direct physiological $CO_2$ effects on ecosystems, among others (IPCC, 2013). Separating these effects is challenging, since some of these processes are plagued by large
30    uncertainties (e.g., land use changes) (IPCC, 2013) or not directly observable at global scale (e.g., carbon uptakes by photosynthesis) (Schimel et al., 2015). The second challenge is that the land sink, as a balance of carbon uptake and release, responds differently to variations in the climatic forcing (Jung et al., 2017; Piao et al., 2020). This makes it hard to attribute induced land sink IAV to specific drivers, which is crucial for process understanding (Jung et al., 2017; Humphrey et al., 2018, 2021). Last, the limited length of observational records may hamper robust statistical analysis (IPCC, 2013): the longest continuous
35    observations of atmospheric $CO_2$ at the South Pole and Mauna Loa observatory exist only since 1958 onwards (Dlugokencky and Tans, 2019).

Land biospheric $CO_2$ uptake results from the net balance of carbon uptake from gross primary productivity, and release from multiple respiration terms, and disturbance induced fluxes such as fires, amongst other smaller terms (IPCC, 2013). Most of these processes are primarily driven by temperature, water and radiation availability (Jung et al., 2017). These meteoro-
40    logical drivers are, in turn, modulated by large–scale modes of atmospheric circulation on multiple time–scales, such as El Niño/Southern Oscillation (ENSO) (Gu and Adler, 2011) and the Pacific Decadal Oscillation (PDO) (Newman et al., 2016). These dynamics are generated within the coupled atmosphere–ocean systems (Ghil, 2002) and considered irreducible noise in climate projections (Madden, 1976; Schneider and Kinter, 1994; Deser et al., 2012). Because these modes typically interact and affect weather dynamics in regions beyond those where they are expressed, such modes are collectively referred to as
45    teleconnections (IPCC, 2013). Bacastow (1976) showed that ENSO is highly correlated with annual variations in observed atmospheric $CO_2$ measured at the South Pole and Mauna Loa, Hawaii. Keeling et al. (1995) attributed these correlations to the ENSO impact on the biospheric sink. In addition to ENSO, Zhu et al. (2017) showed that the PDO and AMO (the Atlantic Multi–decadal Oscillation) may also influence global terrestrial ecosystem carbon fluxes and that other modes of variability in the Northern hemisphere (NH) have also local impacts on carbon cycling (Zhu et al., 2017).
50    A common approach to diagnose the impacts of natural climate variability is to use ensembles of Earth system model simulations with perturbed initial conditions to quantify the impacts of natural climate variability at decadal to millennium scales (Frölicher et al., 2013). However, the inherent chaotic atmosphere system contrasts with model structural uncertainty resulting in large prediction discrepancies among models (Deser et al., 2020). Also, Earth system model projections can be compromised by limited representation of the full complexity of physical processes involved, lack of observational constraints,
55    and high computational demands when aiming to resolve high resolutions (Randall et al., 2007; IPCC, 2013).

Statistical approaches are a simplified but effective way to reveal physical processes in observations (von Storch, 1995). A traditional approach consists of evaluating relationships between the variables of interest (e.g. $CO_2$ time–series) and teleconnection indices (Bacastow, 1976; Bastos et al., 2013; Zhu et al., 2017). As a simple representation of the large–scale atmo-

spheric variability modes, teleconnection indices are extracted mainly from sea surface temperature or atmospheric anomalies

60 (Kumar and Hoerling, 1997; IPCC, 2013). Such indices are an effective way to reduce the complexity of the spatio–temporal variability in multiple variables (Stenseth et al., 2003; Wills et al., 2017), but may not be able to capture spatial variations in the atmospheric modes themselves.

Recently, Sippel et al. (2019) applied Ridge Regression (RR), a regularized linear regression method (Hastie et al., 2009; Friedman et al., 2010), to quantify the component of precipitation and temperature variability driven by atmospheric variations

65 based on sea level pressure (SLP) fields, rather than teleconnection indices. Their approach allowed them to robustly infer the main spatio–temporal patterns of atmospheric variability influencing these two climate variables. On the one hand, including a field of circulation–based predictors, avoids considering predefined assumptions about their spatial configurations as they are common to teleconnection indices, while at the same time compensating for relatively short historical records. The regularization approach, on the other hand, allows to overcome overfitting and multicollinearity issues due to short time series and a very

70 large number of spatial predictors.

In this study, we aim to quantify the fraction of C–cycle IAV influenced by large–scale atmospheric variability. We use observation–based time–series of atmospheric $CO_2$ growth rate ($AGR$) and land $CO_2$ surface fluxes from atmospheric inversions and Dynamic Global Vegetation (DGVMs), as well as the land sink estimated as a residual of other terms in the Global Carbon Budget 2018 (Le Quéré et al., 2018). We additionally compare results with a very long time series (4000 years) of land $CO_2$

75 fluxes simulated by the Community Earth System Model (CESM). In this study, we first evaluate and compare the predictive skill of predictions based on SLP anomaly patterns to that of traditional teleconnection indices (Section 3.1). Next, we analyze and discuss how the C–cycle sensitivity to atmospheric circulation changes from various latitudinal domains (Section 3.2). Finally, we evaluate the sensitivity of the results to the length of the time–series (Section 3.3).

## 2 Data and methods

80 ### 2.1 $CO_2$ datasets for the recent past

We select the $CO_2$ time–series datasets from the Global Carbon Budget (GCB) 2018 version 1.0 (Le Quéré et al., 2018): the atmospheric $CO_2$ growth rate ($AGR$), the land sink from models ($SL_{\mathrm{DGVMs}}$), the residual land sink ($SL_{\mathrm{Resid}}$), and the land sink from two atmospheric inversions.

In the GCB (Le Quéré et al., 2018), the global $CO_2$ balance is calculated based on the carbon emissions from fossil fuel

85 ($FF$) and land use change ($FLUC$), the $AGR$, the carbon uptake by the ocean sink ($SO$) and the land sink ($SL$).

The difference of annual atmospheric $CO_2$ in a given year and the previous year (Ballantyne et al., 2012; Dlugokencky and Tans, 2018; Le Quéré et al., 2018) corresponds to the $AGR$, which is based on direct observations. The $AGR$ is based on the average of well–mixed $CO_2$ measurements at multiple global stations from the US National Oceanic and Atmospheric Administration Earth System Research Laboratory (NOAA ESRL) (Dlugokencky and Tans, 2018).

90 $FF$ emissions are based on inventories, while $FLUC$, $SL$ and $SO$ are estimated by models ($SL_{\mathrm{DGVMs}}$ and $SO$, respectively in Eq. (1)), all of which contain uncertainties (Le Quéré et al., 2018). The total emissions from $FF$ and $FLUC$ minus $AGR$

should equal the total $SO$ and $SL_{\mathrm{DGVMs}}$ (Eq. (1)). Due to uncertainties in modeled land and/or ocean sinks or in land use estimations (Bastos et al., 2020; Hauck et al., 2020), the budget cannot be balanced and thus an imbalance term ($IMB$) is introduced to the budget.

$$FF + FLUC - AGR - SO = SL_{\mathrm{DGVMs}} + IMB = SL_{\mathrm{Resid}} \tag{1}$$

95

The annual land sink of $CO_2$ ($SL_{\mathrm{DGVMs}}$) is the average net biome production (NBP) simulated by 16 dynamic global vegetation model (DGVMs) forced with historical $CO_2$ concentration and climate changes (Le Quéré et al., 2018). The residual land $CO_2$ ($SL_{\mathrm{Resid}}$) is calculated from emissions, $AGR$, and ocean sinks, as described in Eq. (1). $SL_{\mathrm{Resid}}$ corresponds to the balance of the fossil fuel and land–use change emissions and the sinks in the atmosphere and ocean and provides an alternative estimate of the global land sink.

100

The time–series of $AGR_{\mathrm{R}}$, $SL_{\mathrm{DGVMs}}$, and $SL_{\mathrm{Resid}}$ in GCB2018 are provided at annual time–steps over the period 1959–2017. In the following analysis, we invert the $AGR$ time–series ($AGR_{\mathrm{R}}$ for reversed $AGR$ i.e. -1×$AGR$) for sign consistency with the land sink datasets used (defined as a positive flux from the atmosphere to the land).

Additionally, we use the globally aggregated net atmosphere to land $CO_2$ flux (positive sign as a sink in the biosphere) esti-

105 mated from two atmospheric $CO_2$ inversions in GCB2018: the Jena CarboScope $SL_{\mathrm{CarboScope}}$ (Rödenbeck, 2005; Rödenbeck et al., 2018), and the Copernicus Atmosphere Monitoring Service inversion $SL_{\mathrm{CAMS}}$ (Chevallier et al., 2005), which cover the periods 1976–2017 and 1979–2017 respectively. Here we use the global annual $CO_2$ fluxes adjusted for fossil fuel emissions and lateral fluxes from Bastos et al. (2020). The period common to the $CO_2$ time–series (1980–2017) is selected.

### 2.1.1 Sea level pressure

110 We use global monthly mean SLP fields from ERA5 reanalysis with the spatial resolution of $0.25° \times 0.25°$ (Bell et al., 2020), at monthly time–steps and covering the period 1950–1978 (Bell et al., 2020) and 1979–present (Hersbach et al., 2019). The period common to other datasets of 1958–2017 is selected here.

### 2.1.2 Teleconnection indices

In addition to SLP fields, we select 15 teleconnection indices from the atmosphere–ocean variability, Northern Hemisphere

115 (NH), and Southern Hemisphere (SH).

Three important atmosphere–ocean coupled variability modes influence global climate and the C–cycle: the El Niño–Southern Oscillation (SOI), the Pacific Decadal Oscillation (PDO), and the Atlantic Multidecadal Oscillation (AMO) (Zhu et al., 2017).

In the NH, the most relevant indices are: the Arctic Oscillation (AO), the North Atlantic Oscillation (NAO), the Pacific North American pattern (PNA), the East Atlantic (EA), the East Atlantic/Eastern Russia (EAWR), the Scandinavian pattern

120 (SCAND), the Polar/Eurasia (polarEA), and the West Pacific (WP). These indices are calculated and provided by the Climate Prediction Centre (CPC) of the National Oceanic and Atmospheric Administration (NOAA). Excepting AO, these indices are calculated using Rotated Principal Component Analysis (RPCA) (Barnston and Livezey, 1987), based on monthly mean standardized 1000 mbar or 500 mbar geopotential height anomalies between 20° N and 90° N (Barnston and Livezey, 1987;

Zhu et al., 2017) and provided by the NOAA National climate prediction center (CPC, 2008). The detailed information on
125  calculation procedures is described on NOAA CPC (2008).

In the SH, important indices are the Antarctic Oscillation (AAO), the Tropical Atlantic Dipole (TAD), the Dipole Mode
Index (DMI) of the Indian Ocean Dipole, and the Trans Polar index (TPI).

The teleconnection indices used here have been summarized in Table 1. All the indices are provided as monthly means and
selected for the period of 1958-2017, except the AAO which is available for 1979–2017 only.

### 2.1.3 Long–term pre–industrial control simulations for statistical benchmarking

Here we select the SLP fields and global net biome production fields (NBP) from simulations by the Community Earth System
Model (CESM) version 1.2.2 (in the B1850C5CN configuration), which has been used by Stolpe et al. (2019). This experiment
corresponds to a 4000-yr control run. The simulation was run at an atmospheric resolution of $1.9° \times 2.5°$, using the Community
Atmosphere Model version 5 (CAM5.3; (Neale et al., 2012)) with 30 vertical levels. The model consists of fully coupled
135  atmosphere, ocean, sea ice and land surface components (Hurrell et al., 2013; Meehl et al., 2013b), and did not include dynamic
vegetation. This simulation includes no external forcing, so it is ideal to analyze patterns driven by internal variability.

### 2.2 Data pre–treatment

For all historical datasets ($CO_2$ time–series, SLP fields and teleconnection indices), we first remove years corresponding to
volcanic eruptions (1963, 1982, 1983, 1991, 1992). We then pre–treat the datasets as follows: **1)** the long–term trend of $CO_2$
140  time–series was removed by locally weighted scatterplot smoothing (LOWESS) of the annual time–series with fixed window
size of 25 % interval longer than 30 years (1959–2017) and 45 % for shorter period (1980–2017). **2)** The monthly mean
SLP fields are area–weighted and aggregated to $2° \times 2°$, $5° \times 5°$, and $9° \times 9°$ spatial resolution, and the seasonal cycle removed
by subtracting the monthly mean values for each pixel. We then aggregate SLP values in seasonal means for: December of
the previous year to February of each given year (DJF), March–May (MAM), June–August (JJA), and September–November
145  (SON) and further consider DJF and MAM combined (DJF+MAM) so the number of grid points in DJF+MAM is double of
DJF. **3)** For monthly teleconnection indices, we remove the long–term trends by applying the LOWESS as for the SLP fields,
and calculate DJF, MAM, JJA, and SON mean values accordingly, and further include DJF and MAM combined (DJF+MAM)
as treated in SLP. Here, we refer to DJF and MAM as boreal winter and boreal spring.

For the CESM simulations, the SLP fields are originally provided at $1.9° \times 2.5°$ spatial resolution at monthly mean time–steps,
150  which we then resampled to $5° \times 5°$ spatial resolution. Annual mean NBP was calculated from the monthly fields. NBP and
SLP fields were selected for the simulation period 1000–5000 year.

### 2.3 Methods

The overall goal is to characterize variations in the global C–cycle that can be explained by large–scale atmospheric circulation.
Here, the pixel–based time–series of SLP anomalies are used as predictors ($p \geq 800$) of $CO_2$ time–series ($n \leq 54$ years) in a

**Table 1.** Teleconnection indices

| Index | Name | Description | Source |
|---|---|---|---|
| SOI | Southern Oscillation | Monthly sea level pressure anomalies differences (based on 1981–2010 monthly mean) between Tahiti and Darwin, Australia. (McBride and Nicholls, 1983; Ropelewski and Jones, 1987) Downloaded from the NOAA National centers for Environmental Information (NCEI). | https://www.ncdc.noaa.gov/teleconnections/enso/indicators/soi/#soi-calculation |
| PDO | Pacific Decadal Oscillation | Monthly sea surface temperature (SST) variations in the Northeast and tropical pacific Ocean (Mantua et al., 1997; Mantua and Hare, 2002). Using EOF and regression over $20°$–$90°$ N in the Pacific (Mantua et al., 1997). Downloaded from NOAA NCEI. | https://www.ncdc.noaa.gov/teleconnections/pdo/ |
| AMO | Atlantic multi-decadal Oscillation | Monthly Northern Atlantic temperature fluctuations (Rayner et al., 2003; Enfield et al., 2001). Computed by NOAA Physical Science Laboratory (PSL) (using Kaplan SST V2 dataset) from $0°$–$70°$ N (Enfield et al., 2001). The detrended and unsmoothed version is selected. | https://psl.noaa.gov/gcos_wgsp/Timeseries/AMO/ |
| AO | Arctic Oscillation | Characterized by winds circulations near the Arctic around $55°$ N. Calculated by NOAA NCEI, using Empirical Orthogonal Function (EOF) analyzes the monthly mean 1000 millibar height variations over $20°$–$90°$ N (Higgins et al., 2000, 2002). | https://www.ncdc.noaa.gov/teleconnections/ao/ |
| NAO | North Atlantic Oscillation | The Subtropical High and the Subpolar Low difference in sea level pressure (Barnston and Livezey, 1987). Downloaded from NOAA NCEI. | https://www.ncdc.noaa.gov/teleconnections/nao/ |
| PNA | Pacific-North America | Low–frequency Variations in the Northern Hemisphere extratropics (Barnston and Livezey, 1987; Chen and Van den Dool, 2003). Downloaded from NOAA NCEI. | https://www.ncdc.noaa.gov/teleconnections/pna/ |
| EA | East Atlantic | North–south dipole anomalies extending from the east to west North Atlantic, with a similar spatial structure to NAO (Barnston and Livezey, 1987). | https://www.cpc.ncep.noaa.gov/data/teledoc/ea.shtml |
| EAWR | East Atlantic/Western Russia | Distinct by four dominant anomaly centers with positive phase extending Europe and Northern China, negative covering central North Atlantic and North Capspian Sea (Barnston and Livezey, 1987). | https://www.cpc.ncep.noaa.gov/data/teledoc/eawruss.shtml |
| SCAND | Scandinavia | A main anomaly center over Scandinavia, and a opposite weaker sign over western Europe and eastern Russia/western Mongolia (Barnston and Livezey, 1987). | https://www.cpc.ncep.noaa.gov/data/teledoc/scand.shtml |
| PolarEA | Polar/Eurasia | In positive pattern, negative height anomalies in polar region, and positive anomalies in Northern China and Mongolia (Barnston and Livezey, 1987). | https://www.cpc.ncep.noaa.gov/data/teledoc/poleur.shtml |
| WP | West Pacific | Low frequency variability of North Pacific (Barnston and Livezey, 1987). | https://www.cpc.ncep.noaa.gov/data/teledoc/wp.shtml |
| AAO | Antarctic Oscillation | Empirical Orthogonal Function (EOF) was applied to the monthly mean 700hPa height anomalies over $20°$–$90°$ S (Mo, 2000). Calculated by NOAA (CPC, 2008). | https://www.cpc.ncep.noaa.gov/products/precip/CWlink/daily_ao_index/aao/aao.shtml |
| TAD | Tropical Atlantic Dipole | Here we use TSA (Tropical Southern Atlantic Index). Obtained from NOAA Physical Sciences Laboratory (PSL), computed from the monthly SST average anomaly from $0°$–$20°$ S and 10 $°$ E–$30°$ W, HadISST and NOAA OI 1x1 datasets are used (Enfield et al., 1999; Reboita et al., 2021). | https://psl.noaa.gov/data/correlation/tsa.data |
| DMI | Dipole Mode | Obtained from NOAA PSL, based on the sea surface temperature anomaly gradient between the western and the South eastern equatorial Indian Ocean, HadISST1.1 SST is used (Saji and Yamagata, 2003; Reboita et al., 2021). | https://psl.noaa.gov/gcos_wgsp/Timeseries/Data/dmi.had.long.data |
| TPI | Trans Polar | Normalized pressure difference between stations in Hobart and Stanley, Australia (Pittock, 1980, 1984; Jones et al., 1999), data calculated by University of East Anglia http://www.cru.uea.ac.uk/cru/data/tpi/. | https://psl.noaa.gov/gcos_wgsp/Timeseries/TPI/ |

155 linear regression model. However, the small sample size relative to the large number of predictors ($n < p$) can cause severe overfitting problems and result in unstable predictions (Hastie et al., 2009). Moreover, the existing spatial correlations among the neighboring pixels of SLP anomalies might cause multicollinearity among the predictors (von Storch and Zwiers, 1999).

The potential multicollinearity problem results in unstable regression coefficients in least square estimation, and making it difficult to diagnose the most sensitive spatial patterns of predictors (von Storch and Zwiers, 1999).

160    Sippel et al. (2019) applied Ridge Regression (RR) to avoid these overfitting and multicollinearity problems. RR is a regularized linear regression, whose the fundamental principle is to introduce a constraint (hyper–parameter $\lambda$) to regularize the varying regression coefficients in least squares estimation (Hastie et al., 2009; Friedman et al., 2010). The regularized variance comes with a compromise of biased predictions and is addressed as the bias–variance trade–off (Hastie et al., 2009). When selecting the best hyper–parameter $\lambda$, this trade–off is considered to achieve stable (low variance) while slightly biased

165    predictions (Hastie et al., 2009).

Model performance is evaluated by the $R^2$, the Pearson's correlation $R$, and mean squared error (MSE) of the original $CO_2$ time–series against predicted values. Pearson's correlation $R$ is selected as the main measure of predictability. At the same time, $R^2$ is optimized and verified for validity, and the significance $P < 0.05$ is selected. Given the relatively short period ($n <$ 60), here we use leave–one–out (LOO) cross–validation to achieve optimal model training and testing. For each train and test

170    group splitting, we select the train group as all years excluding three consecutive years and the middle year of those three is then selected as the test sample. We excluded the preceding and following year to reduce the potential influence of temporal auto–correlation. Here, we refer to the correlation of RR LOO predicted $CO_2$ time–series with observed values as $\rho_{\mathrm{predictors}}$, where the predictors are either SLP fields ($\rho_{\mathrm{SLP}}$) or teleconnection indices ($\rho_{\mathrm{Tele}}$). The regression coefficients of RR LOO are described as $\omega_{\mathrm{SLP}}$ and $\omega_{\mathrm{Tele}}$ with SLP and teleconnection indices as predictors respectively.

175    A schematic description of the workflow from model training, validation and selection with the selected interval 1959–2017 is shown in Fig. 1. In panel (a), the global maps represent an example of the spatial distribution of SLP with a resolution of $m° \times m°$, where $m$ varies in [2, 5, 9]. Each pixel corresponds to a time–series of SLP, so that $p$ predictors ($x_i$) with $n = 54$ time–steps are defined. Each predictor is assigned a coefficient $\omega_i$ to collectively predict $CO_2$ time–series $Y$, with length $n = 54$. The cost function (Harrington, 2012) is the sum of all the squared errors of training $y_i$ minus estimated $y_i'$ ($x_i^T \omega$, $\omega$ represents

180    the vector of all $\omega_i$). At the same time, the constraint function (Harrington, 2012) suppresses the coefficient variations under a regularized range defined by the hyper–parameter $\lambda$. Panel (b) shows the model training and validation processes. In this study, DJF SLP is in $9° \times 9°$ with $p = 800$. Note that to reduce the heavy computation load, when conducting spatial and temporal sensitivity study as described in Section 2.4, the range of $\lambda$ is lower and with smaller steps than the range and step shown in the Panel (b). For example, when only selecting the tropical domain of SLP, the number of predictors is much less than 800.

185    So the $\lambda$ is selected in range [10, 1000] with a step of 50. When using teleconnection indices instead of SLP anomalies, the predictors are less than 15, the range of $\lambda$ is selected from [1, 200] with a step of 2.

The first step is to divide datasets into train and test groups, as shown in panel (c). The grouped training datasets are then used for model training and tune the best $\lambda$ through 5–folds cross–validation, the best $\lambda$ that achieves the optimal prediction (highest LOO $R^2$) is then selected by the model to predict test datasets. The model then starts another iteration with train and

190    test grouping. Panel (c) describes the LOO train and test grouping, the years before and after the selected test year are removed for each grouping to reduce the impact of temporal auto-correlations in $CO_2$ time–series.

RR (LOO) cross–validation is performed using the Python package Scikit–learn "Ridge" and the $\lambda$ is tuned by Scikit–learn "RidgeCV" (Pedregosa et al., 2011).

## 2.4 Experimental design

195   1. Preliminary dependency tests. To evaluate the robustness of the results for different characteristics of the datasets and methodological choices, we perform several preliminary tests. **1)** Resolution–dependency test: evaluate the sensitivity of results to the SLP spatial resolution under $2°\times2°$, $5°\times5°$, and $9°\times9°$; **2)** Seasonality–dependency test: evaluate the dependence of results on the definition of particular seasons, with each season is the combination of three consecutive months (from November last year to July the given year). **3)** Temporal auto–correlation of the $CO_2$ time–series: to ensure

200   no significant trend remains in the detrended $CO_2$ time–series.

Here we directly use the results following the preliminary dependency test (Appendix A). The spatial resolution does not influence the results considerably (see Appendix A Fig. A1), therefore we select $9\times9°$ SLP spatial resolution given its smaller number of grid points. The seasonal dependency test shows that DJF and MAM are seasonal combinations more representative of boreal winter and spring (see Appendix A Fig. A2). JJA and SON are found to have lower or no

205   predictability to $CO_2$ time–series, therefore, we limit our results to DJF and MAM. As shown in Appendix A Fig. A3, the temporal auto–correlation of all $CO_2$ time–series is mostly less than 0.4 with lag ranging from 1 to 53 years. With a lag of one year, absolute values of auto–correlation are below 0.2, so that we can exclude strong temporal auto–correlation effects.

2. Model training and evaluation. We evaluate the predictability of annual $CO_2$ time–series using SLP anomalies, tele-

210   connection indices, and SOI independently in the DJF, MAM, and DJF+MAM seasons, using the approach described above. We compare Pearson's correlation of observations and predicted values for different periods (1959–2017 and 1980–2017) and show the corresponding RR coefficient distribution maps.

3. Spatial sensitivity study. We evaluate the predictability of historical annual $CO_2$ time–series using DJF SLP anomalies under different spatial domains in periods of 1959–2017 and 1980–2017. Then we use a 30–yr sliding window with

215   annual $AGR_R$ to depict how the predictability under various SLP domains evolves in the period 1959–2017.

4. Temporal sensitivity study. We evaluate the predictability of annual $CO_2$ time–series $AGR_R$, $SL_{DGVMs}$, and CESM using DJF and MAM SLP anomalies under different time intervals. Sliding windows are employed at time intervals of 15, 20, 30, 40 years for historical datasets and CESM, and 100, 500, and 2000 years for CESM only. For the interval of 100 and 500 years, we use the sliding window of a 50 year step, and a 500 year step for the 2000 years interval. The

220   intervals less than 100 years are all in 1 year step. We also evaluate the error rate of the model in each sliding window of 15, 20, 30, and 40 year lengths. The error rate is calculated by the number of invalid predictions that with significance $P > 0.05$ in $\rho_{SLP}$ divided by the number of total predictions within a given window.
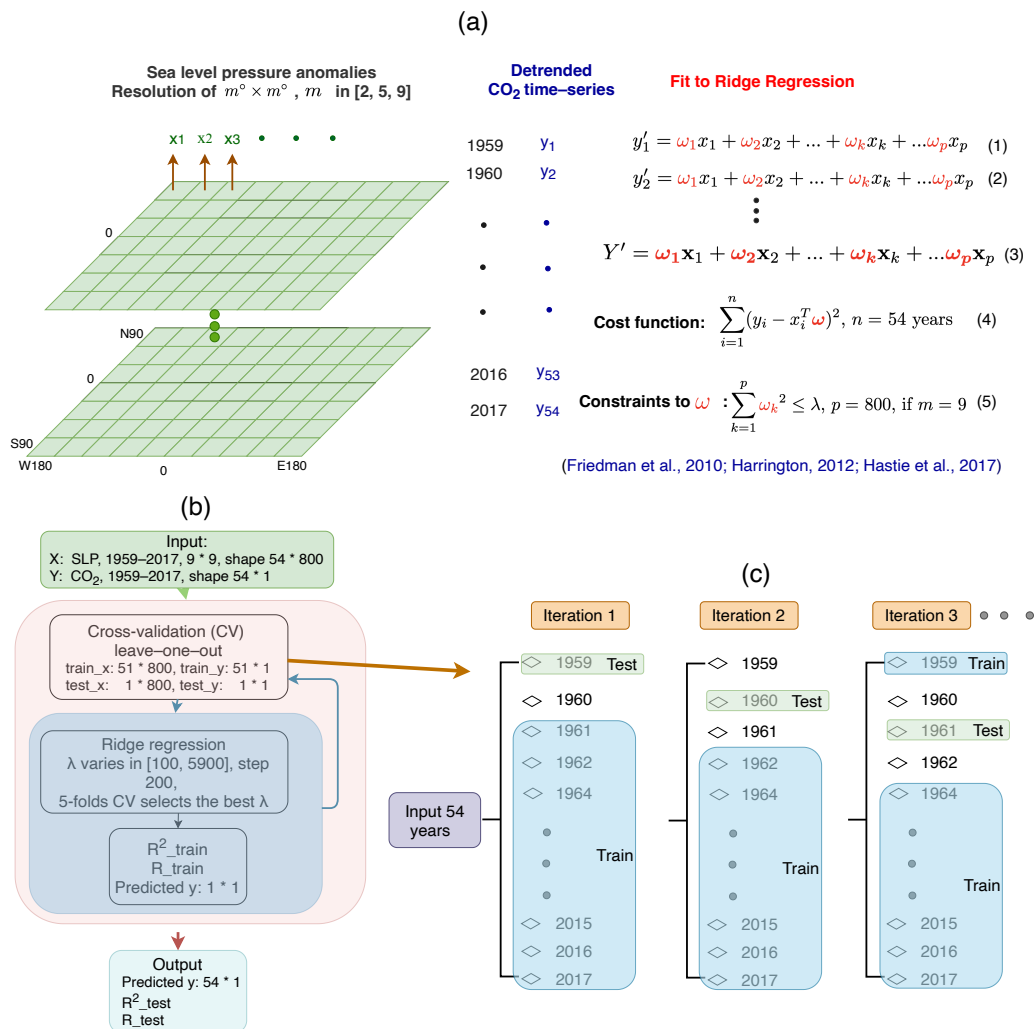
**Figure 1.** Schematic representation of the statistical approach and model design, with an example of the selected time interval of 1959–2017. (a) Fundamental principle of RR. (b) Model training and validation under RR LOO cross–validation. (c) Train and test grouping through LOO.

## 3 Results and discussion

### 3.1 Global IAV patterns

225  In this section, we use the global SLP fields and teleconnection indices as predictors in the RR and, for comparison with other studies, the SOI index as a single predictor in linear regression (LR). We test their predictability to C–cycle IAV with different detrended $CO_2$ time–series, by evaluating the performance of the RR/LR over DJF, MAM and DJF+MAM (Fig. 2).

We find the detrended $CO_2$ time–series are generally consistent with each other, except the $SL_{DGVMs}$ show slight deviation (Fig. 2 a). We find two anomalous years (1987 and 1998), which show deviations larger than 2 standard deviations in most $CO_2$

230  time–series, both signifying apparent $AGR$ increases and subsequent lower land sink (Fig. 2 a). These two years correspond to strong El Niño events, which are usually associated with below–average land $CO_2$ uptake (Keeling et al., 1995; van der Werf et al., 2004; Bonan, 2016).

Here, we refer to the $\rho_{SLP}$ as the LOO correlation of predicted and observed $CO_2$ time–series based on RR and with SLP anomalies as predictors. Accordingly, $\rho_{Tele}$ refers to the LOO correlation that has teleconnection indices as predictors. LOO

235  correlation by linear regression based on the single predictor of SOI index is represented by $\rho_{SOI}$.

SLP and teleconnection indices show comparable predictability of C–cycle IAV in winter, while teleconnection indices have higher predictability in spring (Fig. 2 b). In both periods, the value of $\rho_{SLP}$ (except $SL_{DGVMs}$) is higher in DJF (0.51–0.70) than in MAM (0.29–0.60). On the other hand, the values of $\rho_{Tele}$ are higher in MAM (0.57–0.79) than in DJF (0.53–0.70). The relative low prediction skill of global SLP anomalies compared to teleconnection indices might result from: 1) limited

240  sample size (less than 60 years) and a large number of predictors ($p = 800$) for RR training with global SLP anomalies. But for teleconnection indices and SOI, the predictability skills are much less influenced by the limited sample size due to their limited predictors ($p \leq 15$ for teleconnection indices and $p = 1$ for SOI). As we increase the sample size to over 100 years, the prediction skill of SLP anomalies increases considerably, as is shown in temporal sensitivity study (Fig. 6 a), and 2) the predictability of SLP anomalies in explaining global C–cycle IAV can be reduced in domains with large local rather than global

245  impacts of atmospheric variations to land carbon sinks (Jung et al., 2017). In such domains, the SLP anomalies might show strong relationship to local C–cycle variations but weaker link to global C–cycle variations. Selecting the domains with higher contribution to the global C–cycle variability could improve the predictability, as is shown by the analyzes of sensitivity of the results to the spatial domain (Fig. 4).

Compared to $\rho_{Tele}$, which includes a set of 14 teleconnection indices for period 1959–2017 and 15 for period 1980–2017

250  as predictors, the $\rho_{SOI}$ is slightly lower or similar in both seasons, with 0.53–0.67 in DJF and 0.60–0.74 in MAM (Fig. 2 b). This is consistent with the dominant role of ENSO in driving C–cycle IAV, with other modes showing less contributions. Such interpretation requires caution as the indices cannot fully represent the complex atmospheric dynamics.

The predictability of the combined winter and spring SLP anomalies reveal the different seasonal responses of C-cycle IAV to atmospheric variability (Fig. 2 b). The $\rho_{SLP}$ and $\rho_{Tele}$ in DJF+MAM is within the values for DJF and MAM for most

255  datasets, and slightly higher than the best performing season for $\rho_{SOI}$.
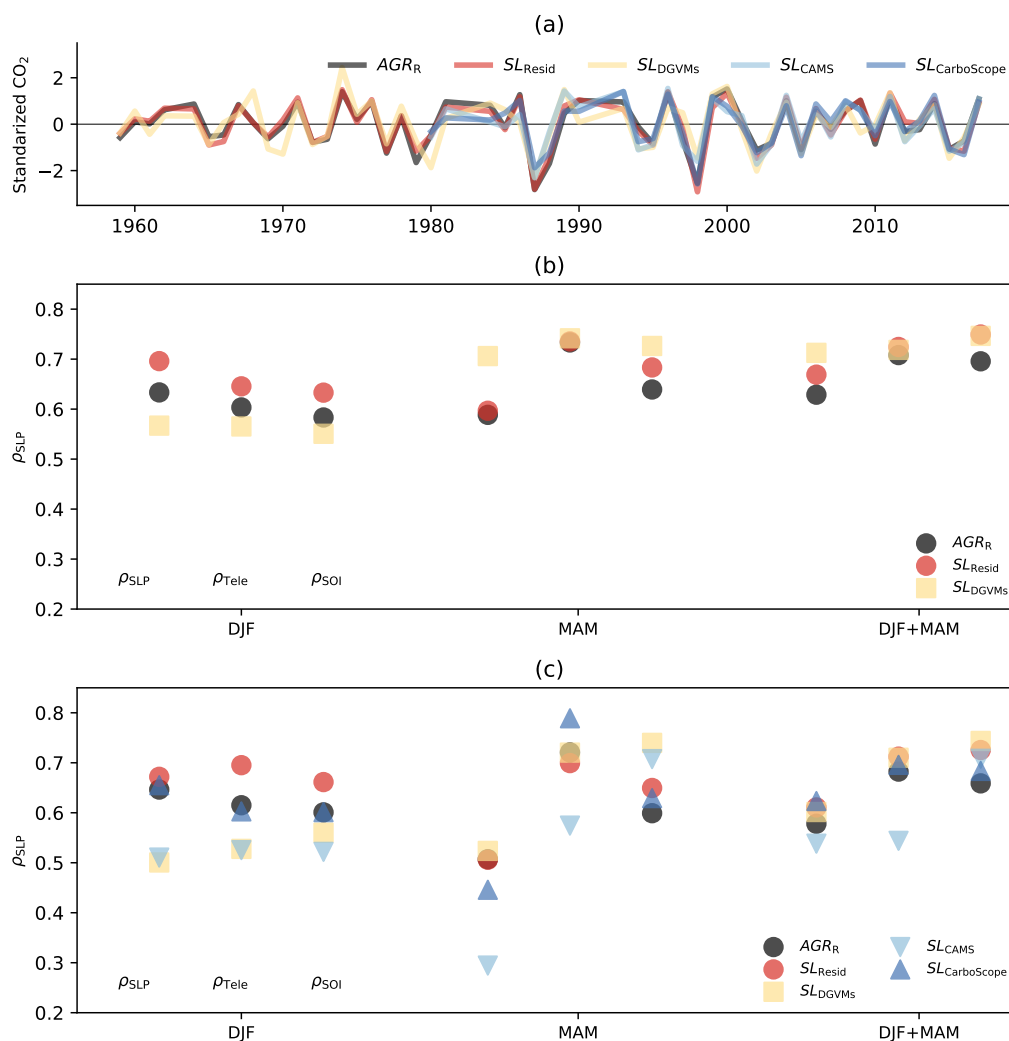
**Figure 2.** (a) Standardized annual $CO_2$ time–series over period 1959–2017 ($AGR_R$ in black, $SL_{Resid}$ in red and $SL_{DGVMs}$ in yellow), and in period 1980–2017 ($SL_{CAMS}$ in light blue and $SL_{CarboScope}$ in dark blue). The $CO_2$ time–series have all been detrended as described in Section 2. Note that the $AGR_R$, $SL_{Resid}$, and $SL_{DGVMs}$ in period 1980–2017 are detrended based on their relevant period, and compared with detrended based on 1959–2017, the difference is negligible. (b) LOO correlation of predicted vs observed $CO_2$ time–series based on the RR with SLP fields ($\rho_{SLP}$) or teleconnection indices ($\rho_{Tele}$) as predictors. Additionally, LOO correlation of $CO_2$ time–series by linear regression based on the single predictor of SOI index ($\rho_{SOI}$). SLP fields, teleconnection indices, and SOI are aggregated for different seasons: DJF, MAM, and DJF+MAM. Panel (b) shows results for 1959–2017 and panel (c) for 1980–2017. Note that in panel (c), the $\rho_{SLP}$ of $SL_{CAMS}$ using MAM SLP as predictor has significance $P = 0.09$, all others have significance $P < 0.05$.

The $\rho_{\text{SLP}}$ of $SL_{\text{Resid}}$ is similar to $\rho_{\text{SLP}}$ of $SL_{\text{DGVMs}}$ in MAM and slightly higher than $\rho_{\text{SLP}}$ of $SL_{\text{DGVMs}}$ in DJF. The difference in the $\rho_{\text{SLP}}$ for $SL_{\text{Resid}}$ and $SL_{\text{DGVMs}}$ in DJF may due to: 1) compared to $SL_{\text{Resid}}$, land sink IAV simulated by DGVMs is less sensitive to DJF climate forcing (Bastos et al., 2018), 2) $SL_{\text{Resid}}$ implicitly includes the variability from land use changes as well as ocean sink variations (Dufour et al., 2013; DeVries et al., 2017; Friedlingstein et al., 2019).

260     We next compare the spatial coefficient patterns of SLP and teleconnection indices in the period of 1959–2017, the results of the period 1980–2017 can be found in Appendix A Fig. A4 and A5.The spatial patterns of the $\omega_{\text{SLP}}$ are similar for the three $CO_2$ time–series: positive coefficients over eastern tropical Pacific Ocean and negative coefficients from Southeast Asia extending to Australia that together roughly consistent with ENSO, and negative from west Pacific (Fig. 3 a). In DJF the negative coefficients over the eastern tropical Pacific are higher than in other regions, while in MAM the area over the central

265 and western tropical Pacific shows higher sensitivity, which are influenced by El Niño and La Niña respectively (Monahan, 2001; Hsieh, 2004; Rodgers et al., 2004; Schopf and Burgman, 2006; Sun and Yu, 2009; Yu and Kim, 2011): El Niño induces negative SLP anomalies over the East Pacific and positive SLP anomalies over the west Pacific (see King et al. (2020), Fig. 5). We infer that the land sink is negatively driven by El Niño in winter (strong El Niño, decreased land sink) and positively driven by La Niña in spring (strong La Niña, increased land sink).

270     The higher $\omega_{\text{Tele}}$ are consistent with the high sensitivity domains of the $\omega_{\text{SLP}}$ corresponding to the patterns of ENSO and WP (Fig. 3, b). Our results show that C–cycle IAV reveals a high positive sensitivity to SOI (0.18 to 0.21) and negative sensitivity to TPI (-0.24 to -0.28) and WP (-0.09 to -0.15) in DJF. High sensitivities are also found for DMI in DJF (negative) and AMO in MAM (negative) (Fig. 3, b). We find that the C–cycle IAV is very sensitive to TPI as well as SOI, which is not so obvious for the spatial patterns of $\omega_{\text{SLP}}$. TPI is a hemispheric–scale index and defined as the pressure anomaly difference between the locations

275 Hobart (43° S, 147 °E) and Stanley (52° S, 58° W) (Pittock, 1980, 1984). We find the TPI to be strongly anti–correlated with SOI in DJF and MAM (-0.89 and -0.85, respectively). This might imply strong atmospheric impacts of ENSO on the C–cycle IAV due to atmospheric variability in SH mid–latitudes.

    However, the observed patterns in $\omega_{\text{Tele}}$ and $\omega_{\text{SLP}}$ need to be interpreted with caution, since these patterns are not necessarily independent from each other. For example, The area from Southeast Asia extending to Australia corresponds to a region

280 influenced by several modes of atmospheric variability: ENSO, the Indian Ocean Dipole (IOD), and the Southern Annular Mode (SAM) (Cleverly et al., 2016). Interactions between these modes have been shown to modulate the occurrence of drought and extreme precipitation in semi–arid areas of Australia, and thus induce large inter–annual variability in gross primary productivity in the region (Cleverly et al., 2016).

    Compared to other $CO_2$ datasets, $SL_{\text{DGVMs}}$ shows higher SLP predictability in MAM rather than DJF (Fig. 2 b). Moreover,

285 $\omega_{\text{SLP}}$ of $SL_{\text{DGVMs}}$ exhibits distinct spatial patterns, especially in DJF, where $\omega_{\text{SLP}}$ for $SL_{\text{DGVMs}}$ is higher in the Southern Pacific rather than over the tropical Pacific region (Fig. 3 a). Compared to historical results, modeled $SL_{\text{DGVMs}}$ show lower predictability in winter rather than in spring, and the spatial patterns of the coefficients for $SL_{\text{DGVMs}}$ are slightly different. These differences might be an indication of shortcomings of DGVMs in simulating the sensitivity of land sink to climatic drivers.
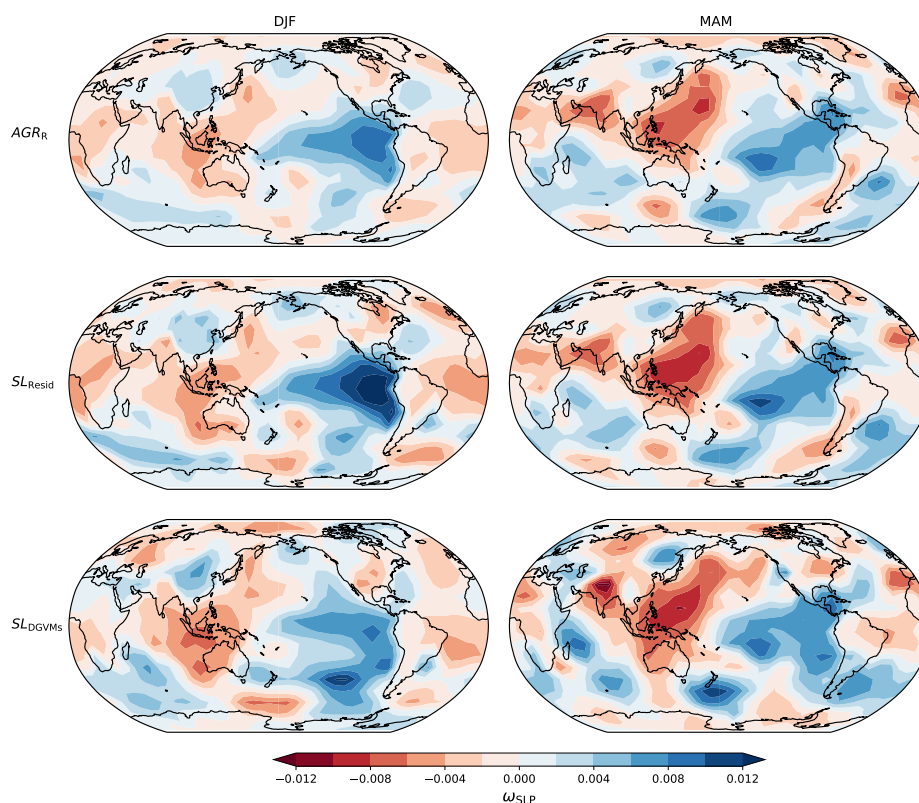
(a)
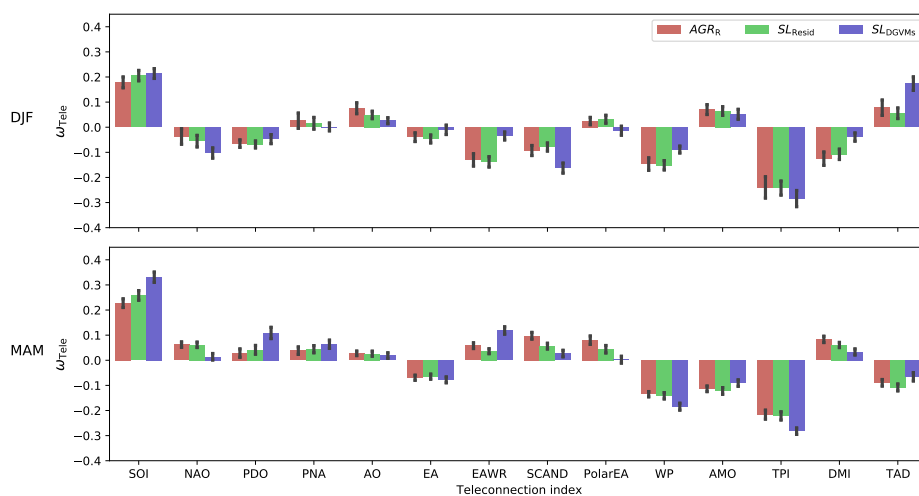
(b)

**Figure 3.** (a) Distribution of $\omega_{\mathrm{SLP}}$ with the time–series of $AGR_{\mathrm{R}}$ (top row), $SL_{\mathrm{Resid}}$ (center row) and $SL_{\mathrm{DGVMs}}$ (bottom row) in DJF (left column) and MAM (right column) based on SLP fields in the period 1959–2017. (b) $\omega_{\mathrm{Tele}}$ of $AGR_{\mathrm{R}}$, $SL_{\mathrm{Resid}}$ and $SL_{\mathrm{DGVMs}}$ based on teleconnection indices. Both $\omega_{\mathrm{SLP}}$ and $\omega_{\mathrm{Tele}}$ are the mean of the $n = 54$ run LOO coefficients.
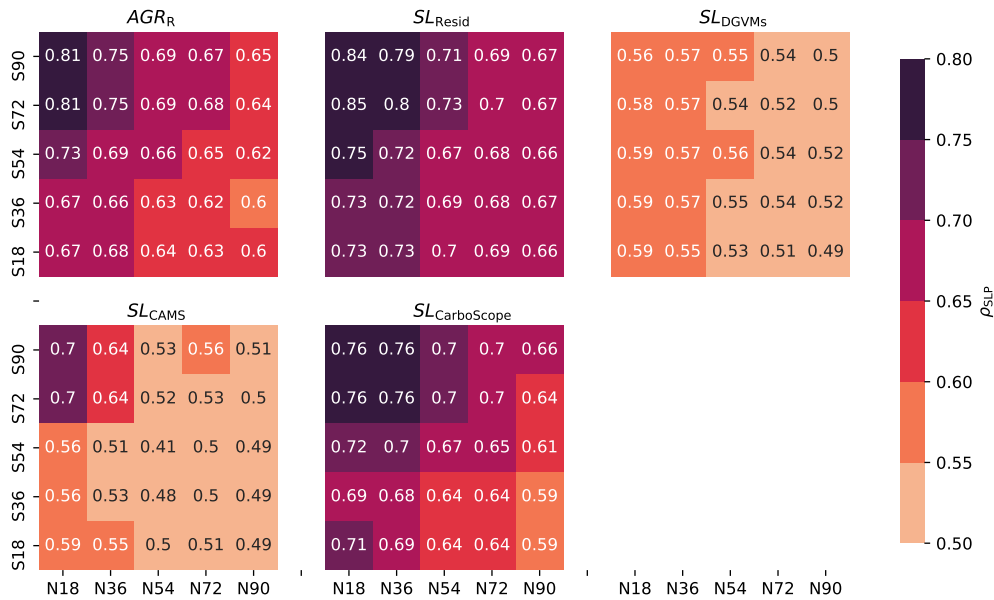
**Figure 4.** Heat map of $\rho_{\mathrm{SLP}}$ with $CO_2$ time–series over various SLP latitude domains in DJF. Each heat map contains 5×5 squares, and each square represents one domain of SLP. For example, the square $36°$ N–$72°$ S is the domain of SLP extending from $36°$ N extending to $72°$ S. All latitudinal domains include the tropical area ($18°$ N–$18°$ S). The top right square thus represents global scale SLP. $\rho_{\mathrm{SLP}}$ of $AGR_{\mathrm{R}}$, $SL_{\mathrm{Resid}}$, $SL_{\mathrm{DGVMs}}$, $SL_{\mathrm{CAMS}}$, and $SL_{\mathrm{CarboScope}}$ in 1980–2017 are shown here.

The general match of spatial patterns from the RR using SLP and the teleconnection indices as predictors of C–cycle IAV indicates that SLP can capture the spatial distribution of the atmospheric patterns that influence IAV, with the advantage of being more flexible than teleconnection indices, since it does not require predefined definitions. However, the short sample size and the large number predictors for RR training hinder the performance of SLP anomalies, especially the lower predictability of SLP anomalies in spring. Reducing the number of predictors (smaller domains of SLP anomalies) or increasing the sample size (longer time interval) for RR training could improve the predictability skill of SLP anomalies. Therefore, in the next subsections, we conduct the spatial and temporal sensitivity of the global C–cycle to SLP anomalies.

### 3.2 Sensitivity to the SLP domains

Here, we test the sensitivity of results to the choice of domain, by evaluating the performance of the RR for DJF and MAM over different latitudinal bands (Fig. 4). We find improved predictability in both seasons when selecting smaller domains (particularly the tropics) rather than global scale of SLP anomalies. Compared to DJF, the sensitivity analysis for $\rho_{\mathrm{SLP}}$ with MAM fields shows lower correlations in general and lower sensitivity to the spatial domain considered. In the following, we

show the results for DJF, the results for MAM can be found in Appendix A Fig. A7. Here we only show the results of the period 1980–2017. The results of the period 1959–2017 show a similar trend (see Appendix A Fig. A6)

Consistent with previous studies (Zeng et al., 2005; Piao et al., 2020), the tropical domain corresponds to higher $\rho_{\mathrm{SLP}}$ for

305   all datasets, but we also find that stronger $\rho_{\mathrm{SLP}}$ are found for regions extending from the tropics to the Southern Hemisphere (SH) (Fig. 4). Including Northern Hemisphere regions (NH) results in lower $\rho_{\mathrm{SLP}}$. The domain 18° N–72° S shows the highest $\rho_{\mathrm{SLP}}$, with $\rho_{\mathrm{SLP}}$ of 0.81 for $AGR_{\mathrm{R}}$ and 0.85 for $SL_{\mathrm{Resid}}$ in 1980–2017.

The results for net atmosphere-land fluxes estimated by atmospheric inversions are consistent with those of $AGR$, with $\rho_{\mathrm{SLP}}$ of 0.70 for $SL_{\mathrm{CAMS}}$ and 0.76 for $SL_{\mathrm{CarboScope}}$ in the same domain of 18° N–72° S. The values of $\rho_{\mathrm{SLP}}$ of $SL_{\mathrm{DGVMs}}$ are

310   systematically lower than the other datasets, independently of the domain.

The weaker values of $\rho_{\mathrm{SLP}}$ when extending SLP domains from tropics to NH (Fig. 4) might be due to the local rather than global impacts of atmospheric variability in NH to land sink IAV. Additional explanations include the fact that carbon fluxes are weaker in winter NH, so that atmospheric variability exerts weaker influence in the global land sink, and that there are strong compensatory effects of gross primary productivity versus terrestrial ecosystem respiration in the NH in response to

315   water and temperature variations (Jung et al., 2017).

The importance of SH atmospheric variability in predicting IAV in $CO_2$ time–series (Fig. 4) is likely due to the strong contribution of semi–arid regions in the SH extratropics to the global sink through their drought/wet anomalies (Poulter et al., 2014; Ahlström et al., 2015), which are controlled by atmospheric variations in the SH (ENSO and ENSO related modes) and to the interactions between ENSO and other modes of atmospheric variability in the SH, such as the synergistic effects from

320   ENSO, IOD and the SAM on Australia C–cycle variability (Cleverly et al., 2016).

### 3.3 Sensitivity to the temporal domains

Because of multi–decadal variability in the climate system, it is possible that the relationships found for short intervals are not stable. In order to investigate whether these results depend on the temporal domain considered, we additionally analyze the results for different temporal domains using a 30–yr interval sliding window (Fig. 5).

325   Results show stronger $\rho_{\mathrm{SLP}}$ of $AGR_{\mathrm{R}}$ confined to the tropics in earlier periods and an intensification of these correlations for the domains extending to the SH over the study period. In some periods, the tropics and Southern extratropics domain shows the highest values of $\rho_{\mathrm{SLP}}$, for example in 1978–2011 and 1984–2015 (Fig. 5). There is, however, high temporal variability in $\rho_{\mathrm{SLP}}$ and of the most relevant spatial domain, with other periods showing higher global coherence (e.g. 1968–2003). It is unclear whether these temporal variations occur randomly due to internal variability in the climate system, or are influenced

330   by external forcing. Potential explanations for this pattern include trends found in SLP and SLP variability over the Pacific and Southern Atlantic (Schneider et al., 2012; IPCC, 2013; Roxy et al., 2019), or enhanced sensitivity of C–cycle variability to climatic drivers, particularly in semi–arid areas, under progressive climate change (Wang et al., 2014; Poulter et al., 2014).

Understanding and attributing these changes to given processes is beyond the scope of this study, but these results highlight the importance of the temporal domain when analyzing IAV in the C–cycle. Since $CO_2$ time–series are short and cover only

335   limited temporal domains, results are likely to be affected by multi–decadal internal climate variability, in addition to external
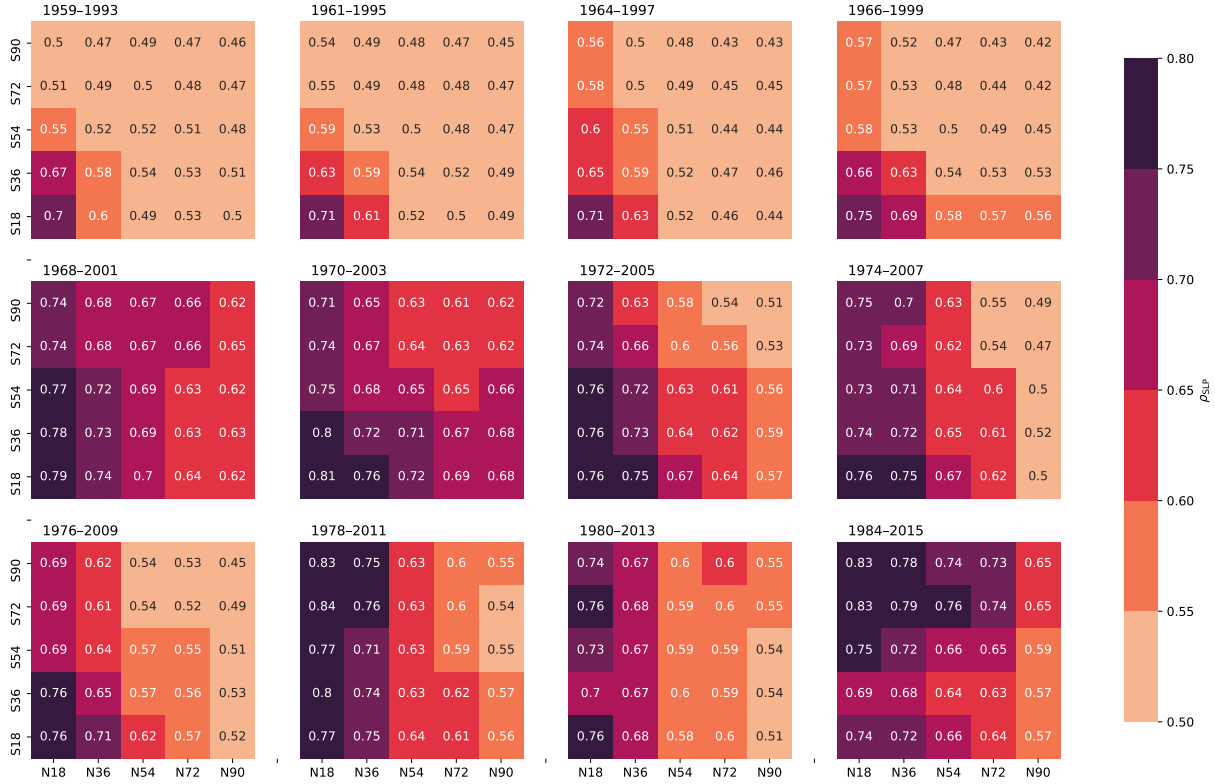
**Figure 5.** $\rho_{\mathrm{SLP}}$ of $AGR_{\mathrm{R}}$ with DJF SLP over various latitude domains. A 30–yr sliding window in the period 1959–2017 with a one year step is created. The starting and end year of each interval is labeled on the top of each heat map. Here we only show the results of every second starting year, the full results are in Appendix A Fig. A9.

forcing. Moreover, the data–driven RR method to quantify circulation–induced C–cycle variability uses a large number of pre-dictors, while only relatively short time series are available for training, which may negatively affect the model's performance. Therefore, we further test the sensitivity of the results to the length of the time–series (Fig. 6). We test the predictability of C–cycle IAV for different lengths of the temporal domain: 15, 20, 30 and 40 years for the datasets in GCB2018 and CESM

340   simulations and 100, 500 and 2000 years for CESM only.

    The boxplots in Fig. 6 show the distribution of $\rho_{\mathrm{SLP}}$ calculated for multiple periods of a given length using a sliding window over the whole period of the respective time–series for the global and tropical domains. The spread of $\rho_{\mathrm{SLP}}$ provides an indication of internal variability in the predictability of C–cycle IAV due to the choice of temporal domain and the uncertainty in the RR fit for a large number of predictors and comparatively small number of training samples.

345   We find that the longer the time interval the higher the mean $\rho_{\mathrm{SLP}}$ and the smaller the variation, i.e. the less dependent are the results on the temporal domain considered (Fig. 6 a). However, the mean value tends to be lower than the median for intervals

shorter than 30 years, and similar to the median for longer intervals. The lower mean is influenced by some domains with very low or even negative $\rho_{\text{SLP}}$ from invalid predictions in shorter time intervals.

The mean $\rho_{\text{SLP}}$ of $AGR_{\text{R}}$ in DJF for the global domain increases from 0.45 to 0.61 from 15–yr to 40–yr respectively, while
350 the spread (maximum - minimum) decreases from 1.04 to 0.18. Results for $SL_{\text{DGVMs}}$ are consistent with those of $AGR_{\text{R}}$, with systematically lower mean $\rho_{\text{SLP}}$ for DJF and higher for MAM, but similar spread in both. The mean values of $\rho_{\text{SLP}}$ for CESM in DJF over the global domain increase from 0.42 (15–yr) to 0.57 (40–yr) and to 0.84 (2000–yr), and the spread decreases from 1.72 to 0.72 and to 0.008, respectively.

At global scale, the predictability of SLP anomalies with $AGR_{\text{R}}$ and with models from $SL_{\text{DGVMs}}$ and CESM are different
355 in winter and spring (Fig. 6 a). $\rho_{\text{SLP}}$ of $AGR_{\text{R}}$ is higher with winter SLP (0.61 in 40–yr DJF), but $\rho_{\text{SLP}}$ of $SL_{\text{DGVMs}}$ and CESM are higher with spring SLP (0.70 and 0.65 in 40–yr MAM).

When limiting the SLP domain to the tropics, results follow the same patterns as those at the global scale, but with better predictive skill: $\rho_{\text{SLP}}$ of $AGR_{\text{R}}$ shows the highest mean correlation of 0.74 for periods of 40 years in DJF (Fig. 6 a). $\rho_{\text{SLP}}$ of $SL_{\text{DGVMs}}$ shows the highest mean predictability, with $\rho_{\text{SLP}}$ of 0.73 for 40–yr MAM (Fig. 6 a), a result that is very similar to
360 those of CESM for the same temporal length ($\rho_{\text{SLP}}$=0.70). We find that with different time scales, tropical SLP in DJF leads to higher predictability of $AGR_{\text{R}}$ than global SLP fields. While the MAM tropical SLP only shows slightly higher predictability than global SLP for $SL_{\text{DGVMs}}$ and CESM.

We find that $AGR_{\text{R}}$ is highly influenced by DJF tropical SLP, while $SL_{\text{DGVMs}}$ and CESM are more sensitive to MAM tropical SLP (Fig. 6). This is consistent with the results of Fig. 4 even when different time scales are considered.

365 However, the Earth system models have been found to not reliably simulate the seasonal timing of ENSO occurrence (Sheffield et al., 2013). The predictability of SLP in seasonal and domain differences between observation data and models could be used as an indicator to reveal their different driving mechanisms.

We evaluate the error rate (i.e., the fraction of predictions in one sliding window with $\rho_{\text{SLP}}$ of significance $P > 0.05$) for $AGR_{\text{R}}$, $SL_{\text{DGVMs}}$, and CESM (see Appendix A Fig. A10). We find that the time interval needed for a robust RR LOO C–cycle
370 IAV prediction is at least about 30 years. For periods shorter than 30 years, the rate of invalid predictions (in the sense given above) can be higher than 40 % for most datasets and SLP domains and seasons. It is worth noting that for $AGR_{\text{R}}$, DJF SLP in the tropical domain still leads to low error rates (13 % in 15–yr), likely due to a smaller number of predictors. From the 15–yr to 30–yr interval, the error rate of $\rho_{\text{SLP}}$ of $AGR_{\text{R}}$ reduces from 0.4 to 0 in DJF global and 0.13 to 0 in DJF tropical. The error rate of $\rho_{SLP}$ decreases to less than 0.16 in 30–yr interval, except $\rho_{SLP}$ of $AGR_{\text{R}}$ decreases to 0.24 in MAM global, which
375 also matches the relative low predictability of MAM SLP anomalies in the period 1980–2017 with different spatial domains (see Appendix A Fig. A7 b). All error rates are reduced to almost zero in a 40–yr interval.

## 4 Conclusions

The major objective of this study was to explore the relationship between SLP anomalies (as a proxy of large–scale atmospheric variations) and the global C–cycle IAV. Specifically, our goals are 1) to investigate the skill of SLP to predict C–cycle IAV

380 using RR and to compare with traditional teleconnection indices, and 2) to reveal how the atmospheric variations influence C–cycle IAV at various spatio–temporal scales.

First, we find that boreal winter and spring SLP anomalies allow predicting IAV of atmospheric $CO_2$ growth rate and IAV of the global land sink. Particularly, with Pearson correlations between detrended $CO_2$ time–series and RR predictions reaching as high as 0.70–0.84 in boreal winter. This is comparable or higher to that of a set of 15 commonly used teleconnection indices.

385 The spatial patterns of coefficients reveal a strong influence of atmospheric variability on C–cycle IAV, particularly due to the El Niño / Southern Oscillation and West Pacific domains. Second, the comprehensive spatio–temporal sensitivity analysis indicates an increasing sensitivity of C–cycle IAV to atmospheric variability during boreal winter in the Southern Hemisphere extratropics in the recent decades. This increased sensitivity may be influenced by internal climate variability or by enhanced sensitivity of C–cycle variability to externally forced changes, but requires further research. Finally, we find that time–series of

390 at least 30 years are needed for robust predictability of C–cycle IAV. For shorter time–series, predictability is highly dependent on the particular period considered, and thus largely due to artifacts of random variability in the fitting process.

Overall, RR provides a novel and efficient data-driven approach for detecting the relationship of atmospheric variations to C–cycle variability. Compared to teleconnection indices, this approach requires no pre–defined spatial configurations and is more flexible on revealing comparable or higher regional prediction skills to C–cycle IAV. This methodology can, therefore,

395 help to improve the detection and attribution of C–cycle variability responses to different driving processes at regional to continental scales.
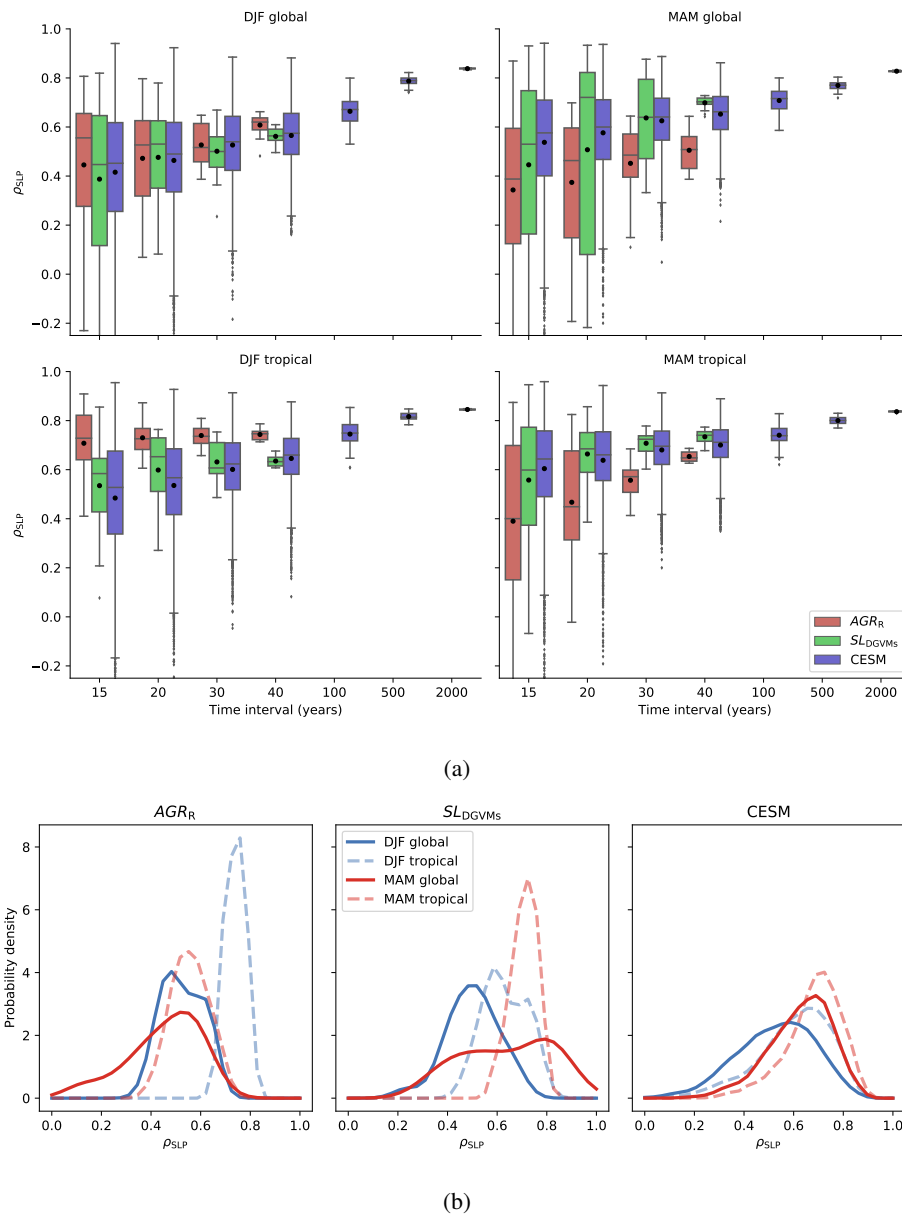
**Figure 6.** $\rho_{\mathrm{SLP}}$ of $AGR_{\mathrm{R}}$, $SL_{\mathrm{DGVMs}}$, and CESM NBP under various time intervals. The $\rho_{\mathrm{SLP}}$ of $AGR_{\mathrm{R}}$ and $SL_{\mathrm{DGVMs}}$ are both within the period 1959–2017, with a 1 year step sliding window of 15, 20, 30, and 40 year. $\rho_{\mathrm{SLP}}$ of CESM in the period 1000–5000 and covers extra intervals of 100, 500, 2000 years. The distribution of the $\rho_{\mathrm{SLP}}$ under each sliding window with SLP in (a): DJF global, MAM global, DJF tropical and MAM tropical. Tropical domains are $18^\circ$ N–$18^\circ$ S for SLP in $\rho_{\mathrm{SLP}}$ of $AGR_{\mathrm{R}}$ and $SL_{\mathrm{DGVMs}}$, and $20^\circ$ N–$20^\circ$ S for SLP in $\rho_{\mathrm{SLP}}$ of CESM. Note that the mean values are in black dots. (b) The distribution of $\rho_{\mathrm{SLP}}$ of $AGR_{\mathrm{R}}$, $SL_{\mathrm{DGVMs}}$ and CESM NBP in a 30–yr sliding window.

**Appendix A**
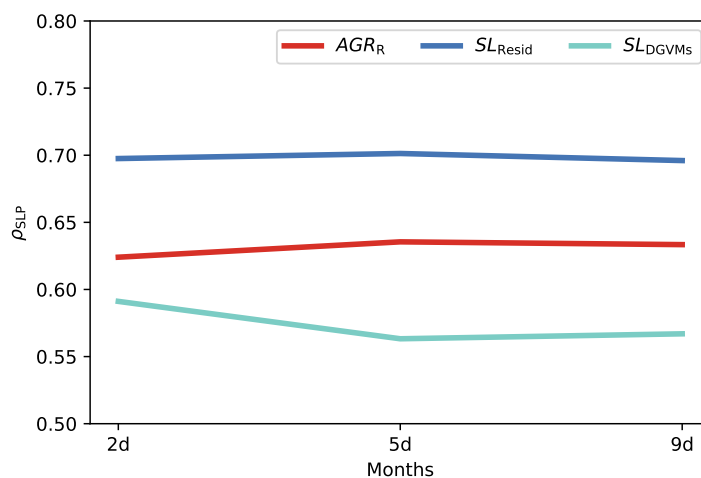
**Figure A1.** $\rho_{\mathrm{SLP}}$ of $AGR_{\mathrm{R}}$, $SL_{\mathrm{Resid}}$ and $SL_{\mathrm{DGVMs}}$ under different DJF SLP resolution ($2° \times 2°$, $5° \times 5°$, $9° \times 9°$) by RR LOO in period of 1959–2017.
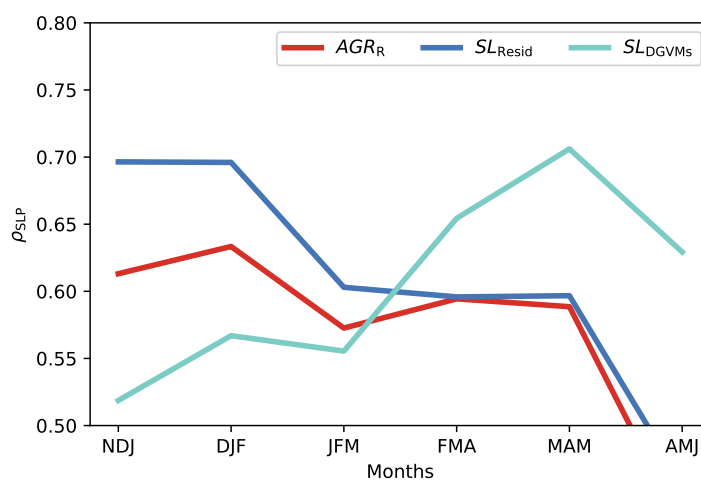
**Figure A2.** $\rho_{\mathrm{SLP}}$ of $AGR_{\mathrm{R}}$, $SL_{\mathrm{Resid}}$ and $SL_{\mathrm{DGVMs}}$ under different seasonal SLP (with different month combination) by RR LOO in period of 1959–2017. Each combination represents: NDJ (November, December, and January), DJF (December, January, and February), JFM (January, February, and March), MAM (March, April, and May), AMJ (April, May, and June).
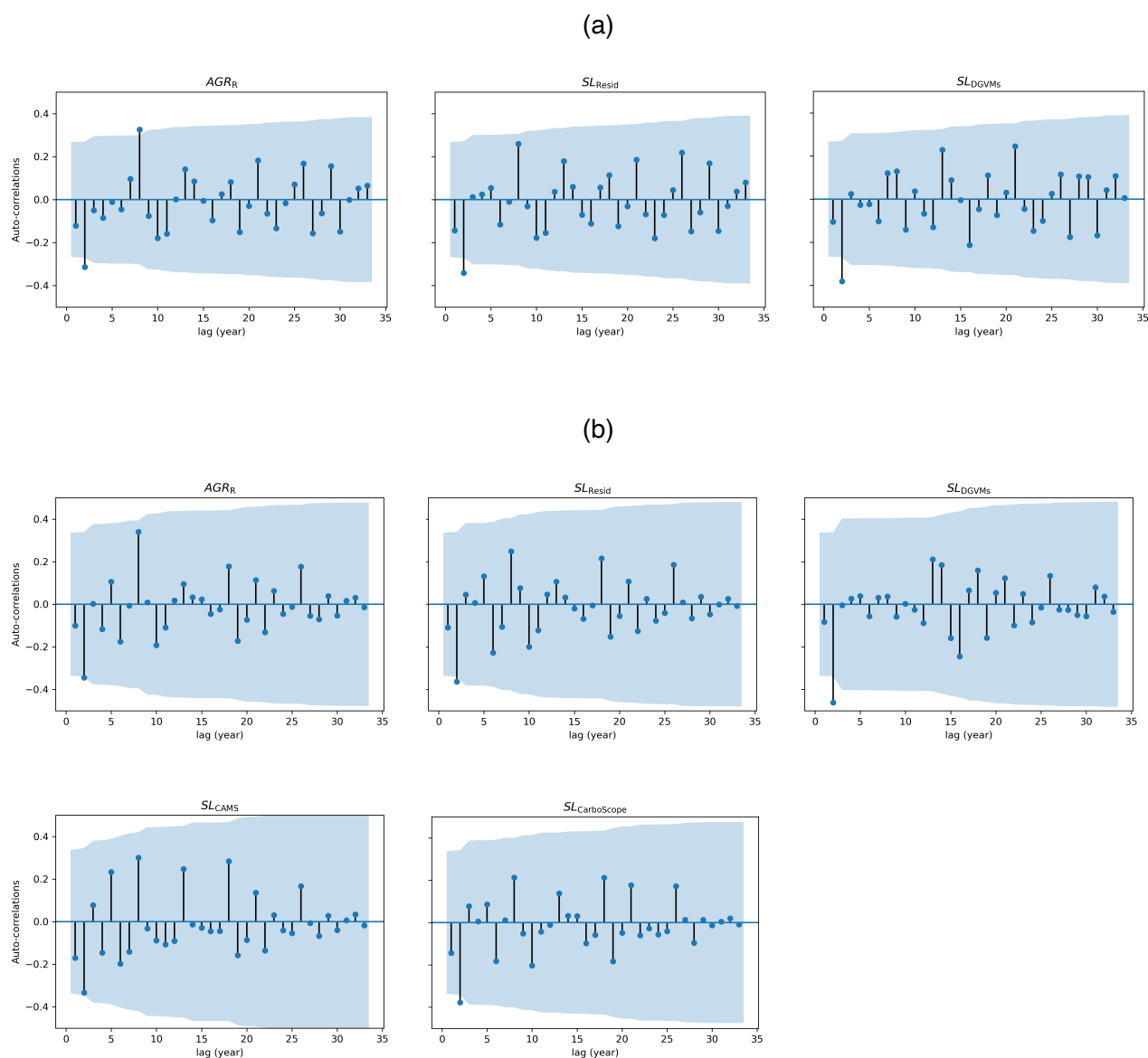
**Figure A3.** Time series auto–correlations of pre–treated $CO_2$ time–series in period (a) 1959–2017 for $AGR_R$, $SL_{Resid}$ and $SL_{DGVMs}$. (b) 1980–2017 included two more inversions $SL_{CAMS}$ and $SL_{CarboScope}$.
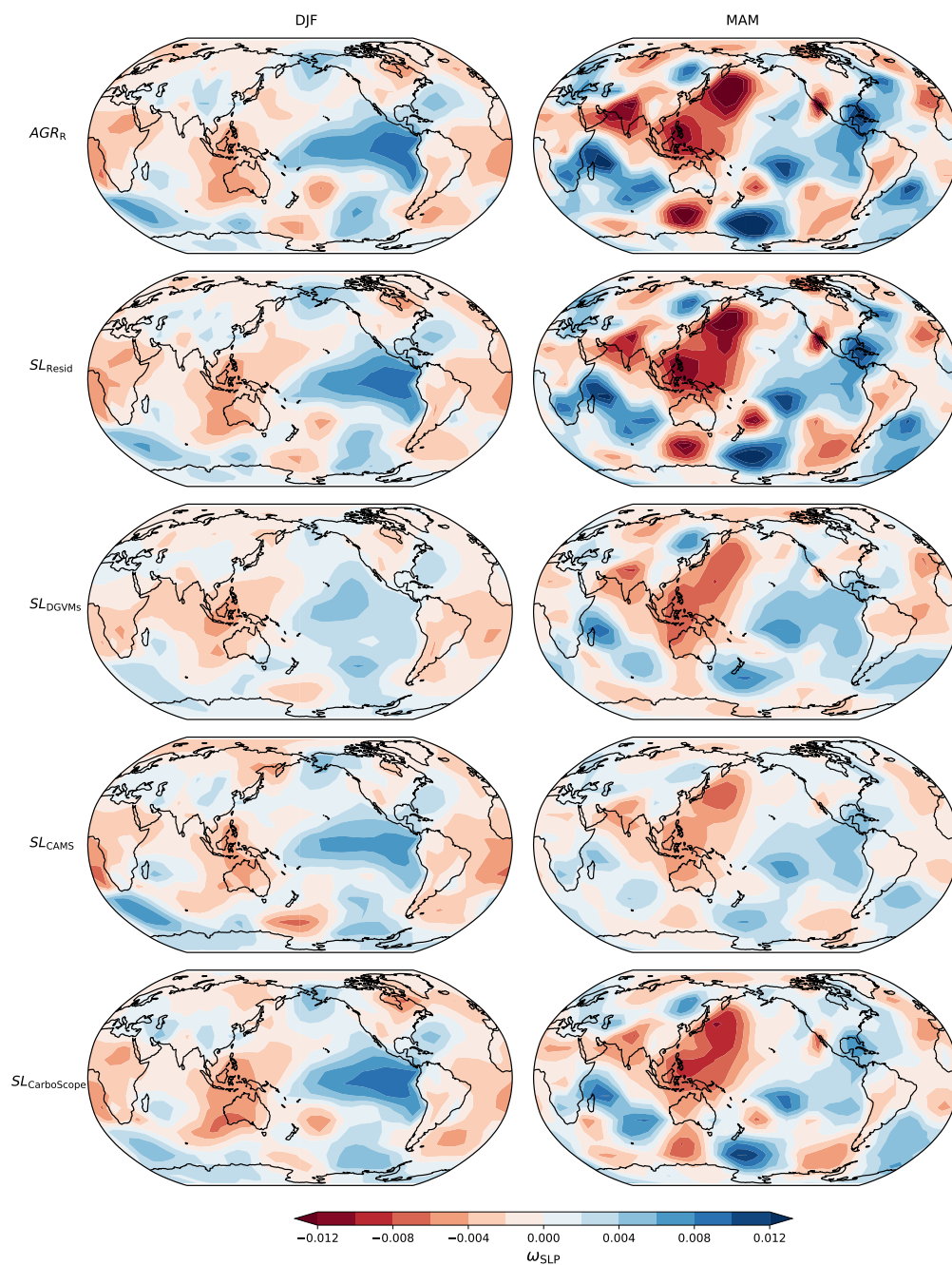
**Figure A4.** Distribution of $\omega_{\mathrm{SLP}}$ with the time–series of $AGR_{\mathrm{R}}$ (top row), $SL_{\mathrm{Resid}}$ (second row), $SL_{\mathrm{DGVMs}}$ (third row), $SL_{\mathrm{CAMS}}$ (fourth row) and $SL_{\mathrm{CarboScope}}$ (last row) in DJF (left column) and MAM (right column) based on SLP fields in the period 1980–2017. $\omega_{\mathrm{SLP}}$ are the mean of the $n = 34$ run LOO coefficients. Note that $\rho_{\mathrm{SLP}}$ of $SL_{\mathrm{CAMS}}$ MAM has $P > 0.5$.
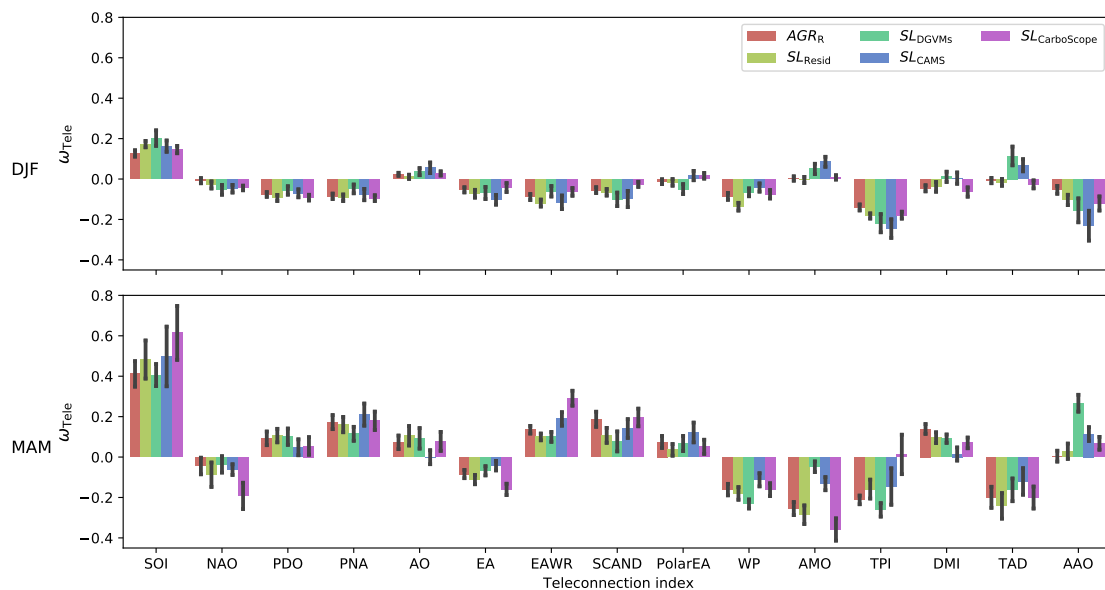
**Figure A5.** Distribution of $\omega_{\text{Tele}}$ with the time–series of $AGR_{\text{R}}$, $SL_{\text{Resid}}$, $SL_{\text{DGVMs}}$, $SL_{\text{CAMS}}$ and $SL_{\text{CarboScope}}$ based on teleconnection indices in period of 1980–2017.
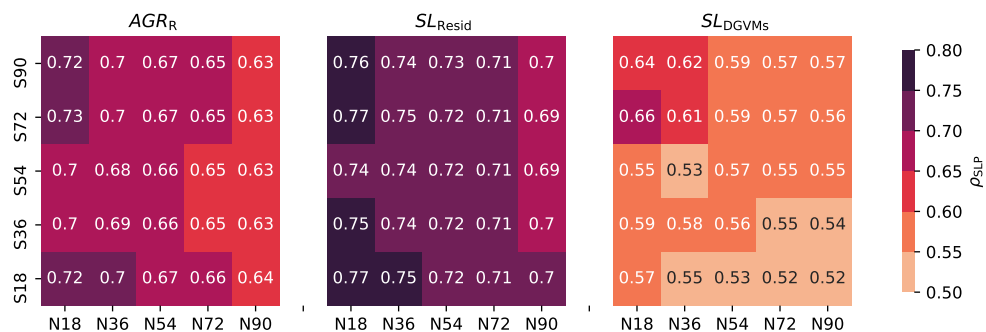
**Figure A6.** Heat map of $\rho_{\text{SLP}}$ with $CO_2$ time–series over various SLP latitude domains in DJF. Each heat map contains 5×5 squares, and each square represents one domain of SLP. For example, the square $36°$ N–$72°$ S is the domain of SLP extending from $36°$ N extending to $72°$ S. All latitudinal domains include the tropical area ($18°$ N–$18°$ S). The top right square thus represents global scale SLP. $\rho_{\text{SLP}}$ of $AGR_{\text{R}}$, $SL_{\text{Resid}}$, $SL_{\text{DGVMs}}$ in 1959–2017.
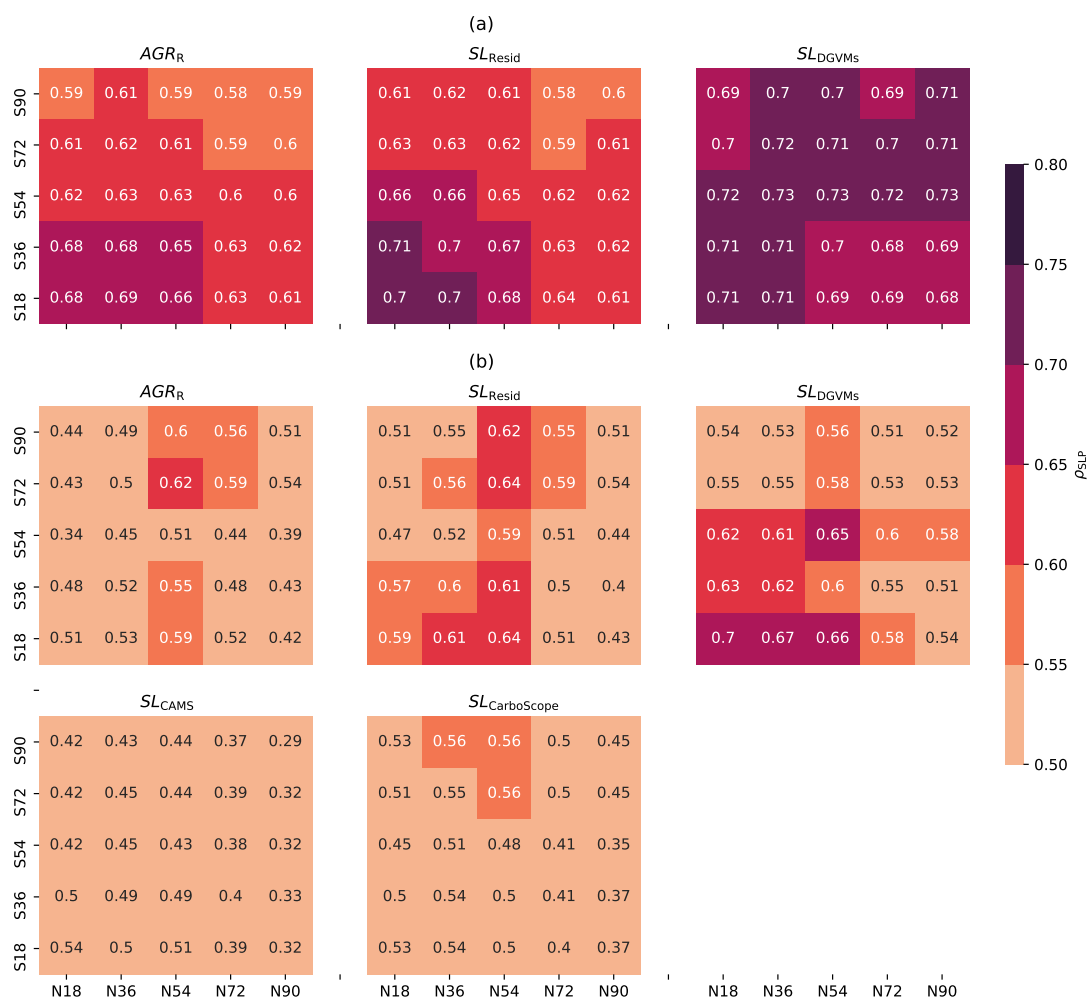
**Figure A7.** Heat map of $\rho_{\text{SLP}}$ with $CO_2$ time–series over various SLP latitude domains in MAM. Each heat map contains 5×5 squares, and each square represents one specific domain of SLP. For example, the square 36° N–72° S is the domain of SLP extending from 36° N extending to 72° S. All latitudinal domains include the tropical area (18° N–18° S). The top right square thus represents global scale SLP. Time series is from (a) 1959–2017 for $AGR_{\text{R}}$, $SL_{\text{Resid}}$ and $SL_{\text{DGVMs}}$. (b) 1980–2017 included two more inversions $SL_{\text{CAMS}}$ and $SL_{\text{CarboScope}}$.
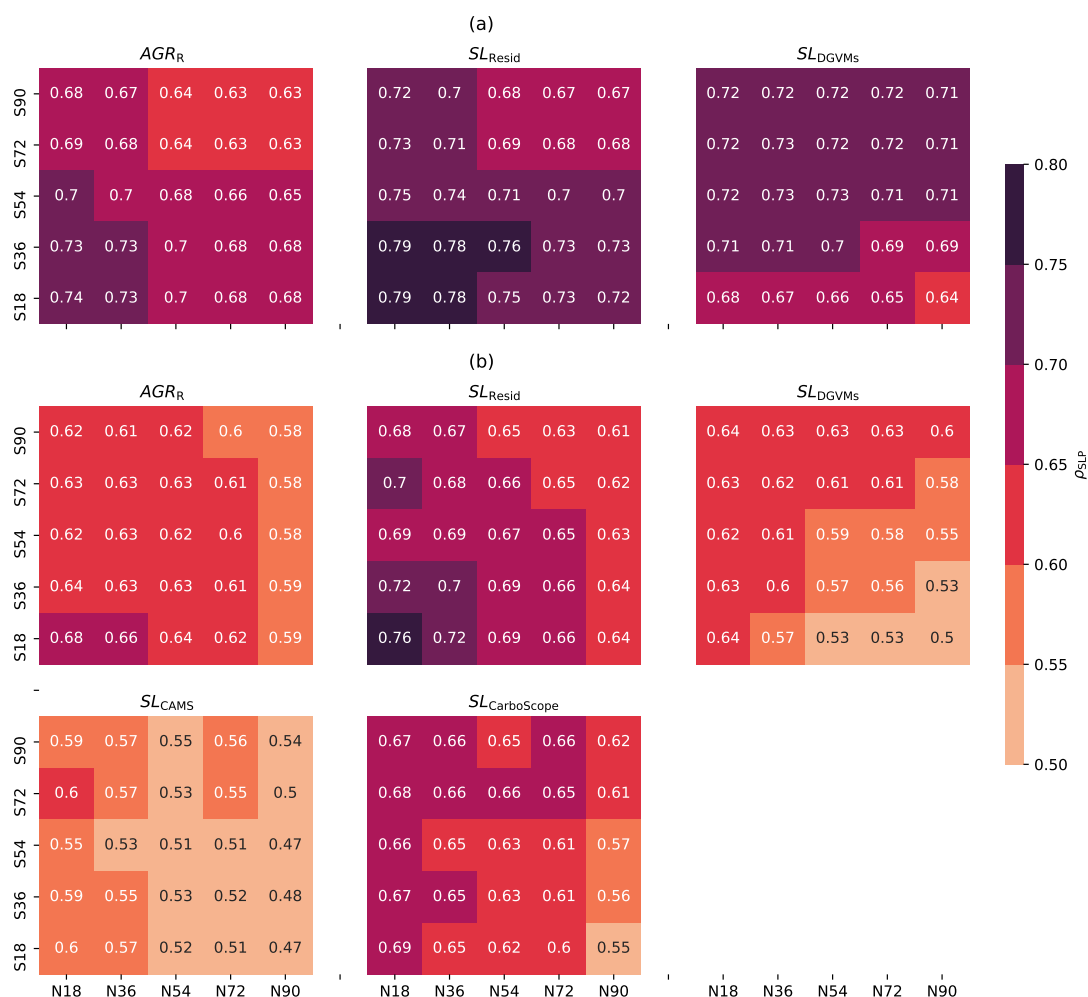
**Figure A8.** Heat map of $\rho_{\mathrm{SLP}}$ with $CO_2$ time–series over various SLP latitude domains in DJF+MAM. Each heat map contains 5×5 squares, and each square represents one specific domain of SLP. For example, the square 36° N–72° S is the domain of SLP extending from 36° N extending to 72° S. All latitudinal domains include the tropical area (18° N–18° S). The top right square thus represents global scale SLP. Time series is from (a) 1959–2017 for $AGR_{\mathrm{R}}$, $SL_{\mathrm{Resid}}$ and $SL_{\mathrm{DGVMs}}$. (b) 1980–2017 included two more inversions $SL_{\mathrm{CAMS}}$ and $SL_{\mathrm{CarboScope}}$.
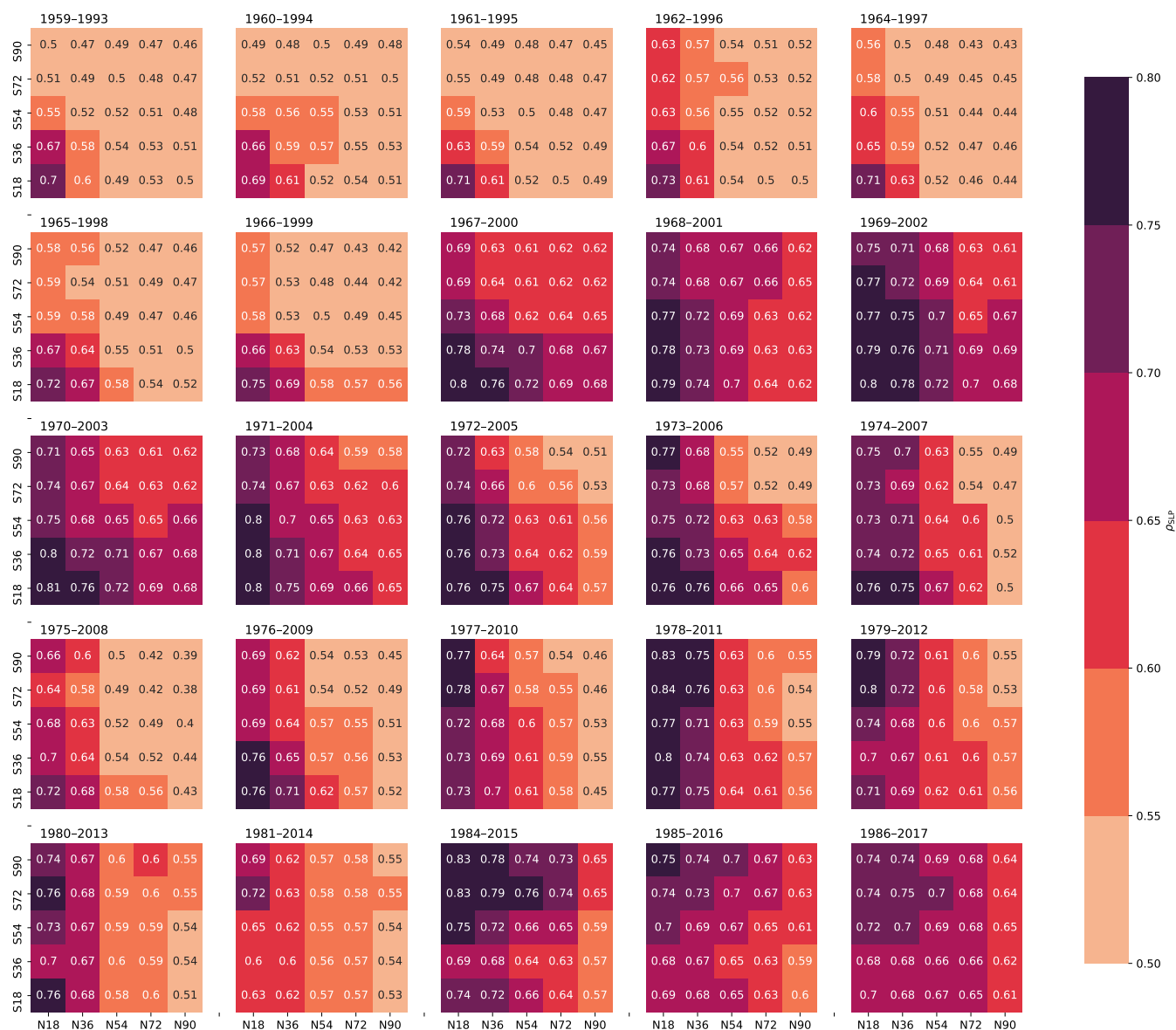
**Figure A9.** Heat map of $\rho_{\mathrm{SLP}}$ of $AGR_{\mathrm{R}}$ with DJF SLP over various latitude domains. A 30–yr sliding window in the period of 1959–2017 with a one year step is created. The starting and end year of each interval is labeled on the top of each heat map.
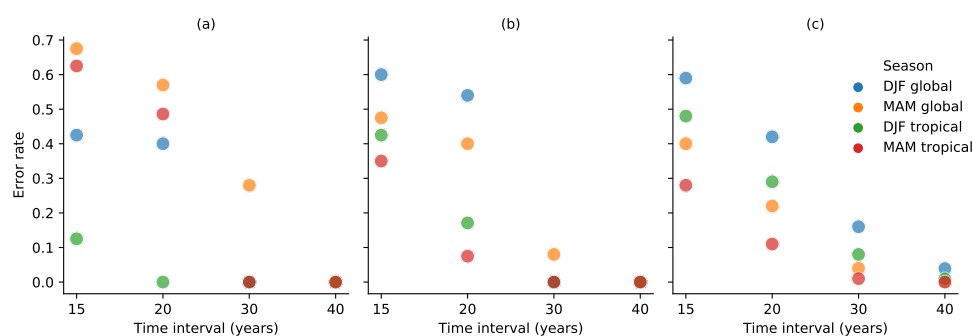
**Figure A10.** Error rate of sliding window in 15, 20, 30 and 40 year intervals. For each sliding window, the error rate is calculated by the number of invalid predictions (with significance $P > 0.05$ in $\rho_{\text{SLP}}$ of $CO_2$ time–series) divided by the number of total predictions. With SLP in DJF global, MAM global, DJF tropical and MAM tropical as predictors, the error rate of $\rho_{\text{SLP}}$ of (a)$AGR_{\text{R}}$, (b) $SL_{\text{DGVMs}}$, and (c) CESM are plotted.

## Appendix B:  Data availability

The Global Carbon Budget 2018 dataset (Le Quéré et al. (2018)) is available at https://www.icos-cp.eu/science-and-impact/
400   global-carbon-budget/2018. The two atmospheric inversion datasets are available in Bastos et al. (2019). The monthly sea level
pressure is from ERA5 reanalysis available at Climate data store, for the period 1959-1978 is from Bell et al. (2020) and the
period 1979-2017 is from Hersbach et al. (2019). The download links for the 15 teleconnection indices are available in Table 1
of Section 2.1.2. The sea level pressure and NBP from CESM1.2 is available in Stolpe et al. (2019).

## Appendix C:  Code availability

405   The Python scripts are available at https://edmond.mpdl.mpg.de/privateurl.xhtml?token=8f717b4f-aea2-4a9b-96a3-efc8487e54af

*Author contributions.*

NL processed the data, performed the analysis and wrote the first draft of the manuscript. SS, AB, MR designed the study.
SS pre-processed the CESM1.2 data. All authors contributed to design the methodology and to the writing of the manuscript.

*Competing interests.*

410   The authors declare that they have no conflict of interest.

*Disclaimer.*

Publisher's note: Copernicus Publications remains neutral with regard to jurisdictional claims in published maps and insti-
tutional affiliations.

*Acknowledgements.*  Markus Reichstein and Alexander J. Winkler acknowledge support by the European Research Council (ERC) Synergy
415   Grant "Understanding and Modelling the Earth System with Machine Learning (USMILE)" under the Horizon 2020 research and innovation
programme (Grant agreement No. 855187).

# References

Ahlström, A., Raupach, M. R., Schurgers, G., Smith, B., Arneth, A., Jung, M., Reichstein, M., Canadell, J. G., Friedlingstein, P., Jain, A. K., Kato, E., Poulter, B., Sitch, S., Stocker, B. D., Viovy, N., Wang, Y. P., Wiltshire, A., Zaehle, S., and Zeng, N.: The dominant role of semi-arid ecosystems in the trend and variability of the land $CO_2$ sink, Science, 348, 895–899, https://doi.org/10.1126/science.aaa1668, 2015.

Bacastow, R. B.: Modulation of atmospheric carbon dioxide by the Southern Oscillation, Nature, 261, 116–118, https://doi.org/10.1038/261116a0, 1976.

Ballantyne, A. P., Alden, C. B., Miller, J. B., Tans, P. P., and White, J. W. C.: Increase in observed net carbon dioxide uptake by land and oceans during the past 50 years, Nature, 488, 70–72, https://doi.org/10.1038/nature11299, 2012.

Barnston, A. G. and Livezey, R. E.: Classification, seasonality and persistence of low-frequency atmospheric circulation patterns, Monthly Weather Review, 115(6), 1083–1126, https://doi.org/10.1175/1520-0493(1987)115<1083:CSAPOL>2.0.CO;2, 1987.

Bastos, A., Running, S. W., Gouveia, C., and Trigo, R. M.: The global NPP dependence on ENSO: La Niña and the extraordinary year of 2011, JGR Biogeosciences, 118, 1247–1255, https://doi.org/10.1002/jgrg.20100, 2013.

Bastos, A., Friedlingstein, P., Sitch, S., Chen, C., Mialon, A., Wigneron, J.-P., Arora, V. K., Briggs, P. R., Canadell, J. G., Ciais, P., Chevallier, F., Cheng, L., Delire, C., Haverd, V., Jain, A. K., Joos, F., Kato, E., Lienert, S., Lombardozzi, D., Melton, J. R., Myneni, R., Nabel, J. E. M. S., Pongratz, J., Poulter, B., Rödenbeck, C., Séférian, R., Tian, H., van Eck, C., Viovy, N., Vuichard, N., Walker, A. P., Wiltshire, A., Yang, J., Zaehle, S., Zeng, N., and Zhu, D.: Impact of the 2015/2016 El Niño on the terrestrial carbon cycle constrained by bottom-up and top-down approaches, Philosophical Transactions of the Royal Society B: Biological Sciences, 373(1760), 20170 304, https://doi.org/10.1098/rstb.2017.0304, pMID: 20808728; PMCID: PMC2929880., 2018.

Bastos, A., Sullivan, M., Ciais, P., Makowski, D., Sitch, S., Friedlingstein, P., Chevalier, F., Rödenbeck, C., Pongratz, J., Luijkx, I., Patra, P., Peylin, P., Canadell, J., Lauerwald, R., Li, W., Smith, N., Peters, W., Goll, D., Jain, A., Kato, E., Lienert, S., Lombardozzi, D., Haverd, V., Nabel, J., Tian, H., Walker, A., and Zaehle, S.: Aggregated regional estimates of net atmosphere-land $CO_2$ fluxes from the five atmospheric inversions and 16 Dynamic Global Vegetation Models, supplemental data to Bastos et al, 2019 (https://doi.org/10.1029/2019GB006393), https://doi.org/10.18160/1SVH-3DNB, 2019.

Bastos, A., O'Sullivan, M., Ciais, P., Makowski, D., Sitch, S., Friedlingstein, P., Chevallier, F., Rödenbeck, C., Pongratz, J., Luijkx, I. T., Patra, P. K., Peylin, P., Canadell, J. G., Lauerwald, R., Li, W., Smith, N. E., Peters, W., Goll, D. S., Jain, A., Kato, E., Lienert, S., Lombardozzi, D. L., Haverd, V., Nabel, J. E. M. S., Poulter, B., Tian, H., Walker, A. P., and Zaehle, S.: Sources of uncertainty in regional and global terrestrial $CO_2$ exchange estimates, Global Biogeochemial Cycles, 34(2), https://doi.org/10.1029/2019GB006393, 2020.

Bell, B., Hersbach, H., Berrisford, P., Dahlgren, P., Horányi, A., Muñoz Sabater, J., Nicolas, J., Radu, R., Schepers, D., Simmons, A., Soci, C., and Thépaut, J.-N.: ERA5 monthly averaged data on pressure levels from 1950 to 1978 (preliminary version), Copernicus Climate Change Service (C3S) Climate Data Store (CDS), https://cds.climate.copernicus.eu/cdsapp#!/dataset/reanalysis-era5-pressure-levels-monthly-means-preliminary-back-extension?tab=overview, last accessed on 17-12-2020, 2020.

Bonan, G. B.: Ecological climatology, concepts and applications, Cambridge University press, 2016.

Chen, W. Y. and Van den Dool, H.: Sensitivity of Teleconnection Patterns to the Sign of Their Primary Action Center, Monthly Weather Review, 131(11), 2885–2899, https://doi.org/10.1175/1520-0493(2003)131<2885:SOTPTT>2.0.CO;2, 2003.

Chevallier, F., Fisher, M., Peylin, P., Serrar, S., Bousquet, P., Bréon, F.-M., Chédin, A., and Ciais, P.: Inferring $CO_2$ sources and sinks from satellite observations: Method and application to TOVS data, J. Geophys. Res., 110, D24 309, https://doi.org/10.1029/2005JD006390, 2005.

Cleverly, J., Eamus, D., Luo, Q., Coupe, N. R., Kljun, N., Ma, X., Ewenz, C., Li, L., Yu, Q., and Huete, A.: The importance of interacting climate modes on Australia's contribution to global carbon cycle extremes, Scientific Reports, 6, https://doi.org/10.1038/srep23113, 2016.

Cox, P. M., Pearson, D., Booth, B. B., Friedlingstein, P., Huntingford, C., Jones, C. D., and Luke, C. M.: Sensitivity of tropical carbon to climate change constrained by carbon dioxide variability, Nature, 494, 341–344, https://doi.org/10.1038/nature11882, 2013.

CPC, N.: NOAA/ National Weather Service NOAA Center for Weather and Climate Prediction, Climate Prediction Center, https://www.cpc.ncep.noaa.gov/data/teledoc/teleindcalc.shtml, last accessed on: August 11, 2021, 2008.

Deser, C., Phillips, A., Bourdette, V., and Teng, H.: Uncertainty in climate change projections: the role of internal variability, Clim Dyn, 38, 527–546, https://doi.org/10.1007/s00382-010-0977-x, 2012.

Deser, C., Lehner, F., Rodgers, K. B., Ault, T., Delworth, T. L., DiNezio, P. N., Fiore, A., Frankignoul, C., Fyfe, J. C., Horton, D. E., Kay, J. E., Knutti, R., Lovenduski, N. S., Marotzke, J., McKinnon, K. A., Minobe, S., Randerson, J., Screen, J. A., Simpson, I. R., and Ting, M.: Insights from Earth system model initial-condition large ensembles and future prospects, Nat. Clim. Change, 10, 277–286, https://doi.org/10.1038/s41558-020-0731-2, 2020.

DeVries, T., Holzer, M., and Primeau, F.: Recent increase in oceanic carbon uptake driven by weaker upper-ocean overturning, Nature, 542, 215–218, https://doi.org/10.1038/nature21068, 2017.

Dlugokencky, E. and Tans, P.: Trends in atmospheric carbon dioxide, National Oceanic  Atmospheric Administration, Earth System Research Laboratory (NOAA/ESRL), http://www.esrl.noaa.gov/gmd/ccgg/trends/global.html, last access: 4 September 2018, 2018.

Dlugokencky, E. and Tans, P.: Trends in atmospheric carbon dioxide, National Oceanic  Atmospheric Administration, Earth Syem Research Laboratory (NOAA/ESRL), http://www.esrl.noaa.gov/gmd/ccgg/trends/global.html, last access on 3 November 2019, 2019.

Dufour, C. O., Le Sommer, J., Gehlen, M., Orr, J. C., Molines, J. M., Simeon, J., and Barnier, B.: Eddy compensation and controls of the enhanced sea-to-air CO2 flux during positive phases of the Southern Annular Mode, Global Biogeochem. Cy., 27, 950–961, https://doi.org/10.1002/gbc.20090, 2013.

Enfield, D. B., Mestas-Nuñez, A. M., Mayer, D. A., and Cid-Serrano, L.: How ubiquitous is the dipole relationship in tropical Atlantic sea surface temperatures?, Journal of Geophysical Research, 104, 7841–7848, https://doi.org/10.1029/1998JC900109, 1999.

Enfield, D. B., Mestas-Nuñez, A. M., and Trimble, P. J.: The Atlantic Multidecadal Oscillation and its relation to rainfall and river flows in the continental U.S., Geophysical Research Letters, 28(10), 2077–2080, https://doi.org/10.1029/2000GL012745, 2001.

Friedlingstein, P., Meinshausen, M., Arora, V. K., Jones, C. D., Anav, A., Liddicoat, S. K., and Knutti, R.: Uncertainties in CMIP5 climate projections due to carbon cycle feedbacks, Journal of Climate, 27(2), 511–526, https://doi.org/10.1175/JCLI-D-12-00579.1, 2014.

Friedlingstein, P., Jones, M. W., O'Sullivan, M., Andrew, R. M., Hauck, J., Peters, G. P., Peters, W., Pongratz, J., Sitch, S., Le Quéré, C., Bakker, D. C. E., Canadell, J. G., Ciais, P., Jackson, R. B., Anthoni, P., Barbero, L., Bastos, A., Bastrikov, V., Becker, M., Bopp, L., Buitenhuis, E., Chandra, N., Chevallier, F., Chini, L. P., Currie, K. I., Feely, R. A., Gehlen, M., Gilfillan, D., Gkritzalis, T., Goll, D. S., Gruber, N., Gutekunst, S., Harris, I., Haverd, V., Houghton, R. A., Hurtt, G., Ilyina, T., Jain, A. K., Joetzjer, E., Kaplan, J. O., Kato, E., Klein Goldewijk, K., Korsbakken, J. I., Landschützer, P., Lauvset, S. K., Lefèvre, N., Lenton, A., Lienert, S., Lombardozzi, D., Marland, G., McGuire, P. C., Melton, J. R., Metzl, N., Munro, D. R., Nabel, J. E. M. S., Nakaoka, S.-I., Neill, C., Omar, A. M., Ono, T., Peregon, A., Pierrot, D., Poulter, B., Rehder, G., Resplandy, L., Robertson, E., Rödenbeck, C., Séférian, R., Schwinger, J., Smith,

N., Tans, P. P., Tian, H., Tilbrook, B., Tubiello, F. N., van der Werf, G. R., Wiltshire, A. J., and Zaehle, S.: Global Carbon Budget 2019, Earth System Science Data, 11, 1783–1838, https://doi.org/10.5194/essd-11-1783-2019, 2019.

Friedman, J., Hastie, T., and Tibshirani, R.: Regularization paths for generalized linear models via coordinate descent, J Stat Softw., 33(1), 1–22, https://doi.org/10.18637/jss.v033.i01, 2010.

Frölicher, T. L., Joos, F., Raible, C. C., and Sarmiento, J. L.: Atmospheric CO2 response to volcanic eruptions: The role of ENSO, season, and variability, Global Biogeochemical Cycles, 27(1), 239–251, https://doi.org/10.1002/gbc.20028, 2013.

Ghil, M.: Natural climate variability, Volume 1, The Earth system: physical and chemical dimensions of global environmental change, from Encyclopedia of Global Environmental Change, John Wiley Sons, Ltd, Chichester, http://citeseerx.ist.psu.edu/viewdoc/download?doi=10.1.1.15.3765&rep=rep1&type=pdf, p544-549, 2002.

Gu, G. and Adler, R. F.: Precipitation and temperature variations on the interannual time scale: Assessing the impact of ENSO and volcanic eruptions, Journal of Climate, 24, 2258–2270, https://doi.org/10.1175/2010JCLI3727.1, 2011.

Harrington, P.: Machine learning in action, Manning publications, p155, 164, 167, 2012.

Hastie, T., Tibshirani, R., and Friedman, J.: The Elements of Statistical Learning: Data Mining, Inferencee, and Prediction, Springer Series in Statistics, https://doi.org/10.1007/b94608, p61-67, 2009.

Hauck, J., Zeising, M., Le Quéré, C., Gruber, N., Bakker, D. C. E., Bopp, L., Chau, T. T. T., Gürses, , Ilyina, T., Landschützer, P., Lenton, A., Resplandy, L., Rödenbeck, C., Schwinger, J., and Séférian, R.: Consistency and challenges in the ocean carbon sink estimate for the Global Carbon Budget, Frontiers in Marine Science, 7, 852, https://doi.org/10.3389/fmars.2020.571720, 2020.

Hersbach, H., Bell, B., Berrisford, P., Biavati, G., Horányi, A., Muñoz Sabater, J., Nicolas, J., Peubey, C., Radu, R., Rozum, I., Schepers, D., Simmons, A., Soci, C., Dee, D., and Thépaut, J.-N.: ERA5 monthly averaged data on pressure levels from 1979 to present, Copernicus Climate Change Service (C3S) Climate Data Store (CDS), https://doi.org/10.24381/cds.6860a573, last accessed on 17-12-2020, 2019.

Higgins, R. W., Leetmaa, A., Xue, Y., and Barnston, A.: Dominant factors influencing the seasonal predictability of U.S. precipitation and surface air temperature, Journal of Climate, 13(22), 3994–4017, https://doi.org/10.1175/1520-0442(2000)013<3994:DFITSP>2.0.CO;2, 2000.

Higgins, R. W., Leetmaa, A., and Kousky, V. E.: Relationships between climate variability and winter temperature extremes in the United States, Journal of Climate, 15(13), 1555–1572, https://doi.org/10.1175/1520-0442(2002)015<1555:RBCVAW>2.0.CO;2, 2002.

Hsieh, W. W.: Nonlinear multivariate and time series analysis by neural network methods, Rev. Geophys., 42, RG1003, https://doi.org/10.1029/2002RG000112, 2004.

Humphrey, V., Zscheischler, J., Ciais, P., Gudmundsson, L., Sitch, S., and Seneviratne, S. I.: Sensitivity of atmospheric $CO_2$ growth rate to observed changes in terrestrial water storage, Nature, 560, 628–631, https://doi.org/10.1038/s41586-018-0424-4, 2018.

Humphrey, V., Berg, A., Ciais, P., Gentine, P., Jung, M., Reichstein, M., Seneviratne, S. I., and Frankenberg, C.: Soil moisture–atmosphere feedback dominates land carbon uptake variability., Nature, 592, 65–69, https://doi.org/10.1038/s41586-021-03325-5, 2021.

Hurrell, J. W., Holland, M. M., Gent, P. R., Ghan, S., Kay, J. E., Kushner, P. J., Lamarque, J.-F., Large, W. G., Lawrence, D., Lindsay, K., Lipscomb, W. H., Long, M. C., Mahowald, N., Marsh, D. R., Neale, R. B., Rasch, P., Vavrus, S., Vertenstein, M., Bader, D., Collins, W. D., Hack, J. J., Kiehl, J., and Marshall, S.: The community earth system model: a framework for collaborative research, Bulletin of the American Meteorological Society, 94, 1339– 1360, https://doi.org/10.1175/Bams-D-12-00121.1, 2013.

IPCC: Climate Change 2013: The Physical Science Basis. Contribution of Working Group I to the Fifth Assessment Report of the Intergovernmental Panel on Climate Change [Stocker, T. F. and Qin, D. and Plattner, G.-K. and Tignor, M. and Allen, S.K. and Boschung,

530      J. and Nauels, A. and Xia, Y. and Bex, V. and Midgley, P.M. (eds.)], Cambridge University Press, Cambridge, United Kingdom and New York, NY, USA, https://www.ipcc.ch/site/assets/uploads/2018/02/WG1AR5_all_final.pdf, p.223, 232, 233, 470, 473, 489, 502, 504,745, 749, 1535, 2013.

Jones, P. D., Salinger, M. J., and Mullan, A. B.: Extratropical circulation indices in the Southern Hemisphere based on station data, International Journal of Climatology, 19, 1301–1317, https://doi.org/10.1002/(SICI)1097-0088(199910)19:12<1301::AID-JOC425>3.0.CO;2-
535      P, 1999.

Jung, M., Reichstein, M., Schwalm, C. R., Huntingford, C., Sitch, S., Ahlström, A., Arneth, A., Camps-Valls, G., Ciais, P., Friedlingstein, P., Gans, F., Ichii, K., Jain, A. K., Kato, E., Papale, D., Poulter, B., Raduly, B., Rödenbeck, C., Tramontana, G., Viovy, N., Wang, Y.-P., Weber, U., Zaehle, S., and Zeng, N.: Compensatory water effects link yearly global land $CO_2$ sink changes to temperature, Nature, 541, 516–520, https://doi.org/10.1038/nature20780, 2017.

540      Keeling, C. D., Whorf, T. P., Wahlen, M., and van der Plichtt, J.: Interannual extremes in the rate of rise of atmospheric carbon dioxide since 1980., Nature, 375, 666–670, https://doi.org/10.1038/375666a0, 1995.

King, M. P., Yu, E., and Sillmann, J.: Impact of strong and extreme El Niños on European hydroclimate, Tellus A: Dynamic Meteorology and Oceanography, 72:1, 1–10, https://doi.org/10.1080/16000870.2019.1704342, 2020.

Kumar, A. and Hoerling, M. P.: Interpretation and implications of the observed inter–El Niño variability, Journal of Climate, 10(1), 83–91,
545      https://doi.org/10.1175/1520-0442(1997)010<0083:IAIOTO>2.0.CO;2, 1997.

Le Quéré, C., Andrew, R. M., Friedlingstein, P., Sitch, S., Hauck, J., Pongratz, J., Pickers, P. A., Korsbakken, J. I., Peters, G. P., Canadell, J. G., Arneth, A., Arora, V. K., Barbero, L., Bastos, A., Bopp, L., Chevallier, F., Chini, L. P., Ciais, P., Doney, S. C., Gkritzalis, T., Goll, D. S., Harris, I., Haverd, V., Hoffman, F. M., Hoppema, M., Houghton, R. A., Hurtt, G., Ilyina, T., Jain, A. K., Johannessen, T., Jones, C. D., Kato, E., Keeling, R. F., Goldewijk, K. K., Landschützer, P., Lefèvre, N., Lienert, S., Liu, Z., Lombardozzi, D., Metzl,
550      N., Munro, D. R., Nabel, J. E. M. S., Nakaoka, S., Neill, C., Olsen, A., Ono, T., Patra, P., Peregon, A., Peters, W., Peylin, P., Pfeil, B., Pierrot, D., Poulter, B., Rehder, G., Resplandy, L., Robertson, E., Rocher, M., Rödenbeck, C., Schuster, U., Schwinger, J., Séférian, R., Skjelvan, I., Steinhoff, T., Sutton, A., Tans, P. P., Tian, H., Tilbrook, B., Tubiello, F. N., van der Laan-Luijkx, I. T., van der Werf, G. R., Viovy, N., Walker, A. P., Wiltshire, A. J., Wright, R., Zaehle, S., and Zheng, B.: Global Carbon Budget 2018, Earth System Science Data, 10, 2141–2194, https://doi.org/10.5194/essd-10-2141-2018, 2018.

555      Madden, R. A.: Estimates of the natural variability of time-averaged sea-level pressure, Monthly Weather Review, 104(7), 942–952, https://doi.org/10.1175/1520-0493(1976)104<0942:EOTNVO>2.0.CO;2, 1976.

Mantua, N. J. and Hare, S. R.: The Pacific Decadal Oscillation, Journal of Oceanography, 58, 35–44, https://doi.org/10.1023/A:1015820616384, 2002.

Mantua, N. J., Hare, S. R., Zhang, Y., Wallace, J. M., and Francis, R. C.: A Pacific interdecadal climate oscillation with im-
560      pacts on salmon production, Bulletin of the American Meteorological Society, 78(6), 1069–1080, https://doi.org/10.1175/1520-0477(1997)078<1069:APICOW>2.0.CO;2, 1997.

McBride, J. L. and Nicholls, N.: Seasonal relationships between Australian rainfall and the Southern Oscillation, Monthly Weather Review, 111(10), 1998–2004, https://doi.org/10.1175/1520-0493(1983)111<1998:SRBARA>2.0.CO;2, 1983.

Meehl, G. A., Washington, W. M., Arblaster, J. M., Hu, A., Teng, H., Kay, J. E., Gettelman, A., Lawrence, D. M., Sander-
565      son, B. M., and Strand, W. G.: Climate change projections in CESM1(CAM5) compared to CCSM4, J. Clim., 26, 6287–6308, https://doi.org/10.1175/jcli-d-12-00572.1, 2013b.

Mo, K. C.: Relationships between low-frequency variability in the Southern Hemisphere and sea surface temperature anomalies, Journal of Climate, 13(20), 3599–3610, https://doi.org/10.1175/1520-0442(2000)013<3599:RBLFVI>2.0.CO;2, 2000.

Monahan, A. H.: Nonlinear principal component analysis: Tropical Indo–Pacific sea surface temperature and sea level pressure, J. Climate, 14, 219–233, https://doi.org/10.1175/1520-0442(2001)013<0219:NPCATI>2.0.CO;2, 2001.

Neale, R. B., Gettelman, A., Park, S., Chen, C. C., Lauritzen, P. H., Williamson, D. L., et al.: Description of the NCAR community atmosphere model (CAM 5.0), NCAR Technical Note (No. NCAR/TN-486+STR), https://doi.org/10.5065/wgtk-4g06, 2012.

Newman, M., Alexander, M. A., Ault, T. R., Cobb, K. M., Deser, C., Lorenzo, E. D., Mantua, N. J., Miller, A. J., Minobe, S., Nakamura, H., Schneider, N., Vimont, D. J., Phillips, A. S., Scott, J. D., and Smith, C. A.: The Pacific Decadal Oscillation, Revisited, Journal of Climate, 29(12), 4399–4427, https://doi.org/10.1175/JCLI-D-15-0508.1, 2016.

Pedregosa, F., Varoquaux, G., Gramfort, A., Michel, V., Thirion, B., Grisel, O., Blondel, M., Prettenhofer, P., Weiss, R., Dubourg, V., Vanderplas, J., Passos, A., Cournapeau, D., Brucher, M., Perrot, M., and Duchesnay, E.: Scikit-learn: Machine Learning in Python, Journal of Machine Learning Research, 12, 2825–2830, 2011.

Piao, S., Wang, X., Wang, K., Li, X., Bastos, A., Canadell, J. G., Ciais, P., Friedlingstein, P., and Sitch, S.: Interannual variation of terrestrial carbon cycle: Issues and perspectives, Global Change Biology, 26, 300–318, https://doi.org/10.1111/gcb.14884, 2020.

Pittock, A. B.: Patterns of climatic variation in Argentina and Chile, I: Precipitation, 1931-60, Monthly Weather Review, 108, 1347–1361, https://doi.org/10.1175/1520-0493(1980)108<1347:POCVIA>2.0.CO;2, 1980.

Pittock, A. B.: On the reality, stability and usefulness of Southern Hemisphere teleconnections, Australian Meteorological Magazine, 32, 75–82, http://www.cmar.csiro.au/e-print/internal/pittock_x1984a.pdf, http://hdl.handle.net/102.100.100/282640?index=1, 1984.

Poulter, B., Frank, D., Ciais, P., Myneni, R. B., Andela, N., Bi, J., Broquet, G., Canadell, J. G., Chevallier, F., Liu, Y. Y., Running, S. W., Sitch, S., and van der Werf, G. R.: Contribution of semi-arid ecosystems to interannual variability of the global carbon cycle, Nature, 509, 600–603, https://doi.org/10.1038/nature13376, 2014.

Randall, D. A., Wood, R. A., Bony, S., Colman, T., Fichefet, T., Fyfe, J., Kattsov, V., Pitman, A., Shukla, J., Srinivasan, J., Stouffer, R. J., Sumiand, A., and Taylor, K. E.: Climate models and their evaluation, In: Climate Change 2007: The Physical Science Basis. Contribution of Working Group I to the Fourth Assessment Report of the Intergovernmental Panel on Climate Change [Solomon, S., D. Qin, M. Manning, Z. Chen, M. Marquis, K. B. Averyt, M. Tignor and H. L. Miller (eds.)] Cambridge University Press, Cambridge, United Kingdomand New York, NY, USA, https://www.ipcc.ch/site/assets/uploads/2018/02/ar4-wg1-chapter8-1.pdf, p589-662, 2007.

Rayner, N. A., Parker, D. E., Horton, E. B., Folland, C. K., Alexander, L. V., Rowell, D. P., Kent, E. C., and Kaplan, A.: Global analyses of sea surface temperature, sea ice, and night marine air temperature since the late nineteenth century, Journal of Geophysical Research: Atmospheres, 108(D104), 4407, https://doi.org/10.1029/2002JD002670, 2003.

Reboita, M. S., Ambrizzi, T., Crespo, N. M., Dutra, L. M. M., de S. Ferreira, G. W., Rehbein, A., Drumond, A., da Rocha, R. P., and de Souza, C. A.: Impacts of teleconnection patterns on South America climate, Annals of the New York Academy of Sciences, https://doi.org/10.1111/nyas.14592, 2021.

Rodgers, K. B., Friederichs, P., and Latif, M.: Tropical Pacific decadal variability and tts relation to decadal modulations of ENSO, Journal of Climate, 17, 3761–3774, https://doi.org/10.1175/1520-0442(2004)017<3761:TPDVAI>2.0.CO;2, 2004.

Ropelewski, C. F. and Jones, P. D.: An extension of the Tahiti–Darwin Southern Oscillation Index, Monthly Weather Review, 115(9), 2161–2165, https://doi.org/10.1175/1520-0493(1987)115<2161:AEOTTS>2.0.CO;2, 1987.

Roxy, M. K., Dasgupta, P., McPhaden, M. J., et al.: Twofold expansion of the Indo-Pacific warm pool warps the MJO life cycle, Nature, 575, 647–651, https://doi.org/10.1038/s41586-019-1764-4, 2019.

605     Rödenbeck, C.: Estimating $CO_2$ sources and sinks from atmospheric mixing ratio measurements using a global inversion of atmospheric transport, Technical Report 6, Max Planck Institute for Biogeochemistry, Jena, http://www.bgc-jena.mpg.de/CarboScope/s/tech_report6.pdf, last accessed on 1 November 2019, 2005.

Rödenbeck, C., Zaehle, S., Keeling, R., and Heimann, M.: How does the terrestrial carbon exchange respond to inter-annual climatic variations? A quantification based on atmospheric $CO_2$ data, Biogeosciences, 15, 2481–2498, https://doi.org/10.5194/bg-15-2481-
610     2018, 2018.

Saji, N. H. and Yamagata, T.: Possible impacts of Indian Ocean Dipole mode events on global climate, Climate Research, 25, 151–169, http://www.jstor.org/stable/24868393, 2003.

Schimel, D., Stephens, B. B., and Fisher, J. B.: Effect of increasing $CO_2$ on the terrestrial carbon cycle, Proceedings of the National Academy of Sciences, 112(2), 436–441, https://doi.org/10.1073/pnas.1407302112, 2015.

615     Schneider, D. P., Okumura, Y., and Deser, C.: Observed Antarctic interannual climate variability and tropical linkages, Journal of Climate, 25, 4048–4066, https://doi.org/10.1175/JCLI-D-11-00273.1, 2012.

Schneider, E. K. and Kinter, J. L.: An examination of internally generated variability in long climate simulations., Climate Dynamics, 10, 181–204, https://doi.org/10.1007/BF00208987, 1994.

Schopf, P. S. and Burgman, R. J.: A simple mechanism for ENSO residuals and asymmetry, Journal of Climate, 19, 3167–3179,
620     https://doi.org/10.1175/JCLI3765.1, 2006.

Sheffield, J., Camargo, S. J., Fu, R., Hu, Q., Jiang, X., Johnson, N., Karnauskas, K. B., Kim, S. T., Kinter, J., Kumar, S., Langenbrunner, B., Maloney, E., Mariotti, A., Meyerson, J. E., Neelin, J. D., Nigam, S., Pan, Z., Ruiz-Barradas, A., Seager, R., Serra, Y. L., Sun, D.-Z., Wang, C., Xie, S.-P., Yu, J.-Y., Zhang, T., and Zhao, M.: North American climate in CMIP5 experiments. Part II: evaluation of historical simulations of intraseasonal to decadal variability, Journal of Climate, 26(23), 9247–9290, https://doi.org/10.1175/JCLI-D-12-00593.1,
625     2013.

Sippel, S., Meinshausen, N., Merrifield, A., Lehner, F., Pendergrass, A. G., Fischer, E., and Knutti, R.: Uncovering the Forced Climate Response from a Single Ensemble Member Using Statistical Learning, Journal of Climate, 32(17), 5677–5699, https://doi.org/10.1175/JCLI-D-18-0882.1, 2019.

Stenseth, N. C., Ottersen, G., Hurrell, J. W., Mysterud, A., Lima, M., Chan, K.-S., Yoccoz, N. G., and Ådlandsvik, B.: Review article.
630     Studying climate effects on ecology through the use of climate indices: the North Atlantic Oscillation, El Niño Southern Oscillation and beyond, Proc. R. Soc. Lond. B., 270, 2087–2096, https://doi.org/10.1098/rspb.2003.2415, 2003.

Stolpe, M. B., Medhaug, I., Beyerle, U., and Knutti, R.: Weak dependence of future global mean warming on the background climate state, Climate Dynamics, 53, 5079–5099, https://doi.org/10.1007/s00382-019-04849-3, 2019.

Sun, F. and Yu, J.-Y.: A 10–15-yr modulation cycle of ENSO intensity, Journal of Climate, 22, 1718–1735,
635     https://doi.org/10.1175/2008JCLI2285.1, 2009.

van der Werf, G. R., Randerson, J. T., Collatz, G. J., Giglio, L., Kasibhatla, P. S., Arellano Jr, A. F., Olsen, S. C., and Kasischke, E. S.: Continental-scale partitioning of fire emissions during the 1997 to 2001 El Niño/La Niña period., Science, 303, 73–76, https://doi.org/10.1126/science.1090753, 2004.

von Storch, H.: Analysis of climate variability applications of statistical techniques, Springer-Verlag Berlin Heidelberg GmbH,
640     https://doi.org/10.1007/978-3-662-03167-4, p10, 1995.

von Storch, H. and Zwiers, W. F.: Statistical analysis in climate research, Cambridge University press, p136, 139, 1999.

Wang, X., Piao, S., Ciais, P., Friedlingstein, P., Myneni, R. B., Cox, P., Heimann, M., Miller, J., Peng, S., Wang, T., Yang, H., and Chen, A.: A two-fold increase of carbon cycle sensitivity to tropical temperature variations, Nature, 506, 212–215, https://doi.org/10.1038/nature12915, 2014.

645    Wills, R. C., Battisti, D. S., Hartmann, D. L., and Schneider, T.: Extracting modes of variability and change from climate model ensembles, in: Proceedings of the 7th International Workshop on Climate Informatics: CI 2017, NCAR Technical Note NCAR/TN-536+PROC, Boulder, USA, https://climate-dynamics.org/wp-content/uploads/2017/12/ci2017_Wills_et_al.pdf, 2017.

Yu, J.-Y. and Kim, S. T.: Reversed spatial asymmetries between El Niño and La Niña and their linkage to decadal ENSO modulation in CMIP3 models, Journal of Climate, 24, 5423–5434, https://doi.org/10.1175/JCLI-D-11-00024.1, 2011.

650    Zeng, N., Mariotti, A., and Wetzel, P.: Terrestrial mechanisms of interannual $CO_2$ variability, Global Biogeochem. Cycles, 19, GB1016, https://doi.org/10.1029/2004GB002273, 2005.

Zhu, Z., Piao, S., Xu, Y., Bastos, A., Ciais, P., and Peng, S.: The effects of teleconnections on carbon fluxes of global terrestrial ecosystems, Geophysical Research Letters, 44, 3209–3218, https://doi.org/10.1002/2016gl071743, 2017.